Prince *et al. Earth, Planets and Space* (2024) 76:85
https://doi.org/10.1186/s40623-024-02015-6

Earth, Planets and Space

FULL PAPER

Open Access

Not too old to rock: ESR and OSL dating reveal Quaternary activity of the Periadriatic Fault in the Alps

Erick Prince[1*], Sumiko Tsukamoto[2,3], Christoph Grützner[1], Marko Vrabec[4] and Kamil Ustaszewski[1]

Abstract

The Periadriatic Fault system (PAF) ranks among the largest post-collisional structures of the European Alps. Recent geodetic data suggest that a fraction of the Adria–Europe convergence is still being accommodated in the Eastern Alps. However, the historical seismicity records along the easternmost segment of the PAF are ambiguous, and instrumental records indicate that seismotectonic deformation is mostly concentrated in the adjacent Southern Alps and Dinarides. Both electron spin resonance (ESR) and optically stimulated luminescence (OSL) dating methods can be used to date coseismic slip (with a combined range covering a few decades to a couple of million years) in slowly deforming fault zones, such as the PAF. Since the saturation doses of the quartz ESR signals are larger than quartz and feldspar OSL, ESR enables establishing a maximum age of the last resetting event of the system, while OSL allows constraining their minimum age when the signal is in saturation. We collected fault gouge samples from three localities along the easternmost segment of the PAF. For ESR, we measured the signals from the Al center in quartz comparing the results from the single aliquot additive dose (SAAD) and single aliquot regenerative (SAR) dose protocols. For OSL, we recorded the infrared stimulated luminescence signal at 50°C (IR_{50}) and post-infrared infrared-stimulated luminescence signal at 225 °C ($pIRIR_{225}$). Our dating results indicate that the studied segment of the PAF system accommodated seismotectonic deformation during the Quaternary, with a maximum age for the last resetting event of the system ranging from 1075 ± 48 to 552 ± 26 ka (ESR SAR) and minimum ages in the range from 196 ± 12 to 281 ± 16 ka (saturation of $pIRIR_{225}$). The obtained ages suggest that the studied segment of the PAF could be considered at least as a potentially active fault.

Keywords Periadriatic fault system, Eastern Alps, Electron spin resonance, Optically stimulated luminescence, Active fault

*Correspondence:
Erick Prince
erick.prince@uni-jena.de
Full list of author information is available at the end of the article

Springer Open

© The Author(s) 2024. **Open Access** This article is licensed under a Creative Commons Attribution 4.0 International License, which permits use, sharing, adaptation, distribution and reproduction in any medium or format, as long as you give appropriate credit to the original author(s) and the source, provide a link to the Creative Commons licence, and indicate if changes were made. The images or other third party material in this article are included in the article's Creative Commons licence, unless indicated otherwise in a credit line to the material. If material is not included in the article's Creative Commons licence and your intended use is not permitted by statutory regulation or exceeds the permitted use, you will need to obtain permission directly from the copyright holder. To view a copy of this licence, visit http://creativecommons.org/licenses/by/4.0/.

Graphical abstract

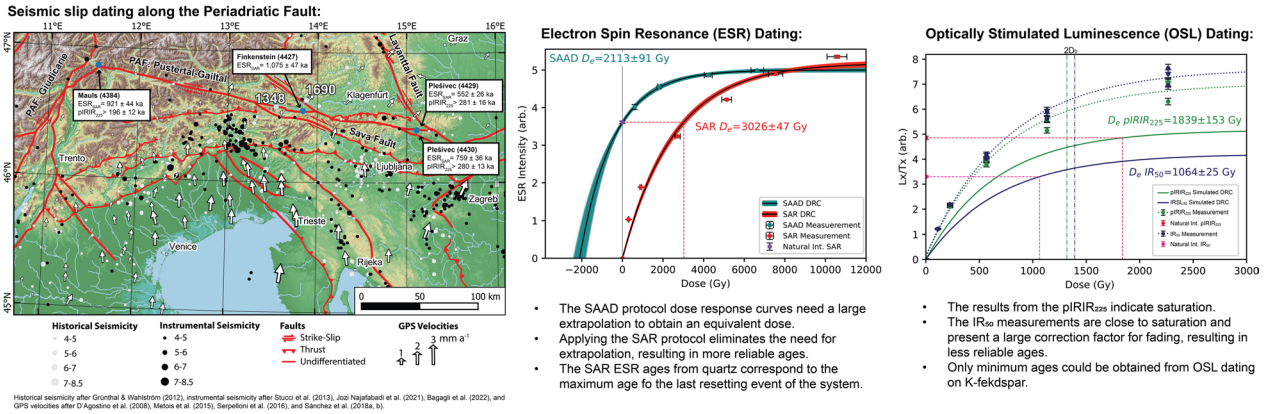

Introduction

This article deals with the Quaternary activity of one of the longest faults in the European Alps that has not had strong instrumental earthquakes (i.e., recorded via instruments). A recurring problem in characterizing past and present regional deformation patterns in many regions is constraining the timing of fault activity. Notwithstanding purely academic aspects, the identification and characterization of active faults (e.g., in terms of slip rates and recurrence rates of damaging earthquakes) are of paramount importance from a societal perspective to assess the regional seismic hazard. Instrumental earthquake records do not necessarily help to identify active faults, and geodetic monitoring may fail to recognize active fault segments in case of locked faults and low deformation rates. The problem may be exacerbated by long or unknown recurrence rates of large earthquakes in regions with low overall deformation rates such as the Alps and the Dinarides (Cheloni et al. 2014; Hintersberger et al. 2018; Grützner et al. 2021; Oswald et al. 2022), or intra-continental regions (e.g., 1811–1812 New Madrid earthquakes: Tuttle et al. 2002; 2001 Gujarat earthquake: Rajendran et al. 2008; 2016 Petermann Ranges Earthquake: King et al. 2021).

To date, there is no single definition for an "active fault". According to the review of Slemmons & McKinney (1977), the most accepted definition is "*a structure that shows evidence of Holocene displacement*", which conflicts in terms of temporal resolution with faults that have recurrence intervals of tens of thousands of years (Machette 2000; Grützner et al. 2016, 2017). Four main criteria presented in Slemmons & McKinney (1977) and originally proposed by Willis & Wood (1924) could be used to assess the activity of a structure. These are either (1) offset during the present tectonic regime (i.e., configuration of the tectonic plate movements and interactions), (2) the potential for future offset, (3) evidence of recent activity, and (4) associated earthquake activity. Other definitions have been provided by the U. S. N. R. Commission (1997), which classifies a tectonic structure as of interest for seismic hazard when there is geological evidence for recurring deformation within approximately the last 0.5 Ma, at least once in the past 50 ka, or when it has been involved in deformation associated with the current tectonic regime. The I. A. E. Agency (2010) proposes guidelines to distinguish active structures depending on the tectonic setting, considering an Upper Pleistocene–Holocene time frame in interplate regions and a Pliocene–Quaternary time frame in intraplate regions.

Since instrumental data acquired via seismometers, satellite images, and Global Navigation Satellite Systems (GNSS) is only available for the last few decades, dating of recent brittle deformation can help determine whether a fault is (potentially) active. The most common techniques for finding the age of brittle deformation episodes in fault zones are either dating deformation associated with earthquakes in displaced or deformed soft sediments with luminescence or radiocarbon methods (e.g., McCalpin 2009; Kondo et al. 2022), dating aseismically formed precipitations such as calcite veins and fibers using ^{230}U/Th (e.g., Nuriel et al. 2012), or K/Ar dating of authigenic illite in fault gouge (e.g., Kralik et al. 1987; Pleuger et al. 2012; Torgersen et al. 2014; Ring et al. 2017; Vrolijk et al. 2018). However, these techniques either suffer from temporal limitations or rely on relative means to date the deformation episodes.

In geoscience, both electron spin resonance (ESR) in quartz and optically stimulated luminescence (OSL) in quartz and feldspar have been applied for dating sediments (e.g., OSL: Wintle and Huntley 1982; Preusser et al. 2008; Mahan et al. 2022; ESR: Schellmann et al. 2008; Tsukamoto et al. 2018; Richter et al. 2022), and recently applied also as ultra-low temperature thermochronometers (e.g., Guralnik et al. 2015; Fang and Grün, 2020; King et al. 2020). These methods utilize unpaired electrons trapped within crystal lattice defects in minerals and measure a signal proportional to the accumulation over time by exposure to natural irradiation (Rink 1997; Aitken 1998). The trapped charges can be released either during periods of increased temperature due to shear heating, elevated stress (normal or shear), and frictional grain comminution (Fukuchi 1992; Yang et al. 2019). Therefore, they potentially allow direct dating of seismotectonic deformation in fault zones at near-surface conditions (e.g., Ikeya et al. 1982; Fukuchi 1992; 2001).

In this work, we present the first attempt to apply direct dating methods to constrain active deformation along the Periadriatic Fault system (PAF) in the European Alps, by combining quartz ESR and feldspar OSL dating retrieved from fault gouges sampled in the core zone of the structure. The PAF represents an orogen-scale post-collisional fault system that was active mostly in the Oligocene to Miocene, but whose Quaternary activity is not well understood. Large instrumental earthquakes have not occurred on this fault system, and the historical earthquake records are ambiguous (Hammerl et al. 1994; Guidoboni et al. 2019; Caracciolo et al. 2021; Kázmér et al. 2023). Given the potential of the ESR and OSL dating methods to directly constrain the timing for seismogenic faulting episodes in the Quaternary, especially for slow-moving faults that are potentially still active, the PAF provides an opportunity to study the last seismogenic activity. For ESR, we compare the measurements and ages obtained with the single aliquot regenerative (SAR) dose protocol and the single aliquot additive dose (SAAD) protocol. For OSL, we employ the post-infrared infrared-stimulated luminescence (pIRIR) protocol, with infrared (IR) stimulations at 50 °C and 225 °C. Our findings indicate that at least a partial reset of the system was achieved during the Quaternary due to seismogenic faulting along the sampled portions of the structure.

The Periadriatic Fault system

The PAF system is an orogen-scale array of post-collisional, predominantly dextral, and mostly transpressive strike-slip faults in the European Alps. It formed in response to the NW motion and counterclockwise rotation of the Adriatic plate with respect to Europe during the Alpine orogeny (Schmid et al. 1989; Fig. 1). The fault system can be traced for about 700 km along-strike the entire width of the orogen, starting from N of Turin, Italy, to the Pannonian Basin in Hungary where it becomes buried below Plio–Pleistocene basin sediments. The eastern PAF system (east of the Giudicarie Fault) also represents the division between the high-grade metamorphic Austroalpine units to the north and the low-grade South Alpine units to the south (Fig. 2). A suite of calc–alkaline intrusive bodies, usually referred to as Periadriatic plutons, occurs along much of the length of the PAF. These plutons are considered to have resulted from a magmatic episode triggered by slab breakoff of the southward subducting European plate during the Eocene–Oligocene (von Blanckenburg and Davies 1995; Rosenberg 2004).

According to different estimates, the PAF could have accommodated between 150 and 300 km of displacement between about 35 and 15 Ma (Laubscher 1971; Schmid et al. 1989; Schmid & Kissling 2000; Handy et al. 2005). The structure contributed to lateral extrusion in the Eastern Alps towards the Pannonian Basin during the late Oligocene–Miocene (Ratschbacher et al. 1991a, b). The northward motion of the southern Alpine indenter (the rigid northern tip of the Adriatic microplate) between 22 and 17 Ma led to an offset on the PAF by the NNE–SSW-trending sinistral Giudicarie Fault, modifying the originally straight E–W trend of the structure defined by the Insubric and Pustertal–Gailtal segments (e.g., Viola et al. 2001; Pomella et al. 2012; Sieberer et al. 2023; Fig. 1a). The minimum age for the offset has been established by K/Ar dating targeting clay minerals in fault gouges by Pleuger et al. (2012), which indicates displacement along the segment at around 17 Ma. This offset was simultaneous with south-directed thrusting in the eastern Southern Alps (Schönborn 1999; Castellarin and Cantelli 2000; Verwater et al. 2021). The post-Oligocene displacement along the PAF segments east of the Giudicarie Fault possibly did not exceed about 20 km (Ustaszewski et al. 2008), and was concurrent with at least 40–50 km N–S convergence accommodated along south-directed thrusts in the easternmost Southern Alps in Friuli (Nussbaum 2000; Merlini et al. 2002; Moulin & Benedetti 2018).

The Neogene deformation along the Pustertal–Gailtal segment of the PAF system has a prominently dextral transpressive character, especially in the region of the Karawanken Mountains (Polinski and Eisbacher 1992; Nemes et al. 1997; Fodor et al. 1998; Vrabec and Fodor 2006; Fig. 2a). In this segment, shortening is accommodated by slip partitioning between dextral strike-slip faults and N- and S-directed thrusts. On the northern edge of the Karawanken Mountains, Mesozoic successions overthrust the Middle Miocene to Pliocene sedimentary infill of the Klagenfurt basin (Polinski & Eisbacher 1992; Nemes et al. 1997;

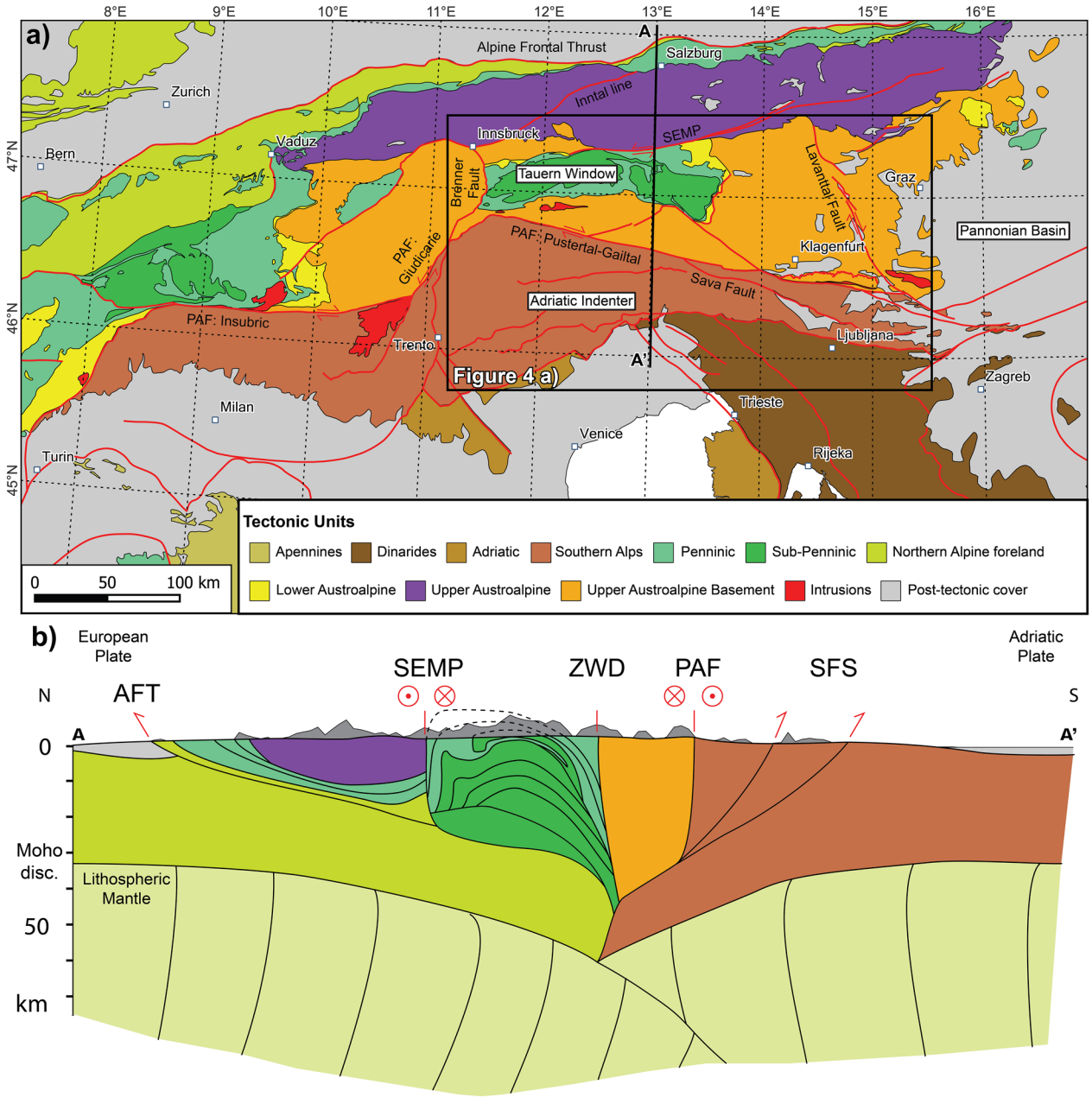

Fig. 1 **a** Tectonic map of the Alps. Modified after Schmid et al., (2004). **b** Simplified N–S-trending cross section across the Alps at 13° E showing the structural position of the different tectonic units (black lines delimit the boundaries between the units) and main structures with their respective kinematics (red lines). Fault zones: AFT Alpine Foreland Thrust, PAF Periadriatic Fault, SFS Sangone Fault System, SEMP Salzach–Ennstal–Mariazell–Puchberg Fault, ZWD Zwischenbergen–Wöllatratten and Drautal Faults. Modified after Schmid et al. (2013) and Hetényi et al. (2018)

Fig. 2b). Apatite (U–Th–Sm)/He ages obtained along the fault fall between around 12 and 5 Ma and indicate Late Miocene to Pliocene cooling below 110–50 °C, likely triggered by fault-related basement exhumation (Heberer et al. 2017). K/Ar dating of clay minerals in fault gouges hints at displacement along the structure in the westernmost part of the segment (Mauls, Italy) at around 16 Ma (Zwingmann & Mancktelow 2004).

Available GNSS data (D'Agostino et al. 2008; Métois et al. 2015; Serpelloni et al. 2016; 2022; Sánchez et al. 2018a, b) suggest that a part of the present NW–SE convergence between stable Adria and Europe is still being accommodated along contractional faults in

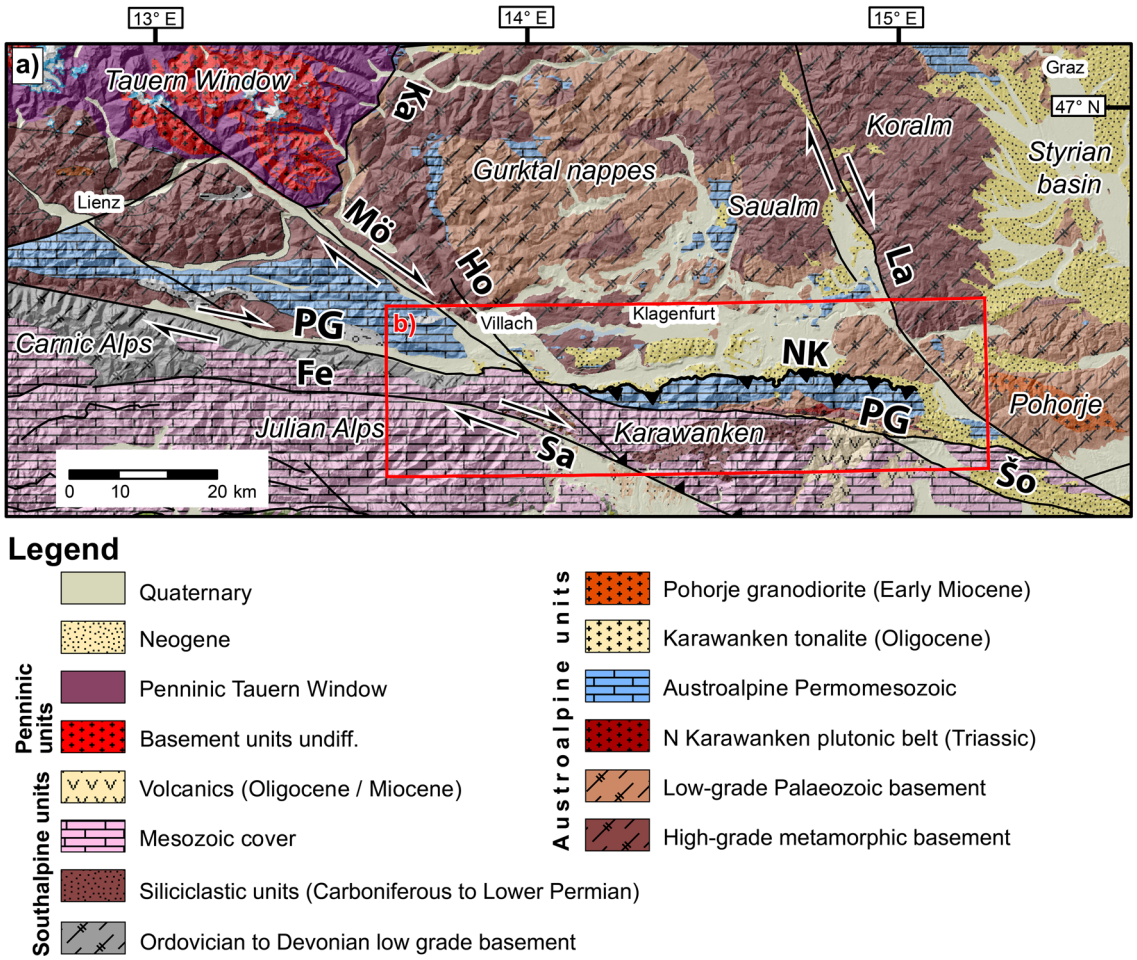

Fig. 2 **a** Simplified geological map of the Pustertal–Gailtal segment of the PAF. Modified after Heberer et al. (2017). Fault zones: Fe Fella Fault, Ho Hochstuhl Fault, La Lavanttal Fault, Mö Mölltal Fault, NK North Karawanken Thrust, PG Pustertal–Gailtal Fault, Sa Sava Fault, Šo Šoštanj Fault. **b** Detail of the Pustertal–Gailtal segment of the PAF in the Karawanken mountains

the Southern Alps and across the eastern PAF (vectors in Fig. 3). Still, the seismic moment release along the eastern PAF system is considerably smaller than in the Southern Alps of Friuli, located south of the structure (Serpelloni et al. 2016; Reiter et al. 2018). It is also possible that this segment of the PAF system hosted a few strong historical earthquakes, such as the Mw~7.0 event in 1348 and the Mw~6.6 event in 1690 (AHEAD Group: Albini et al. 2013; Guidoboni et al. 2019), both with epicenters in Carinthia. However, recent studies place the epicenter to the south of the PAF towards Friuli (Hammerl 1994; Caracciolo et al. 2021). In a recent archaeoseismology study, Kázmér et al. (2023) inferred a damaging earthquake at the eastern tip of the PAF near Celje (Slovenia) in the fourth century AD based on deformed Roman buildings.

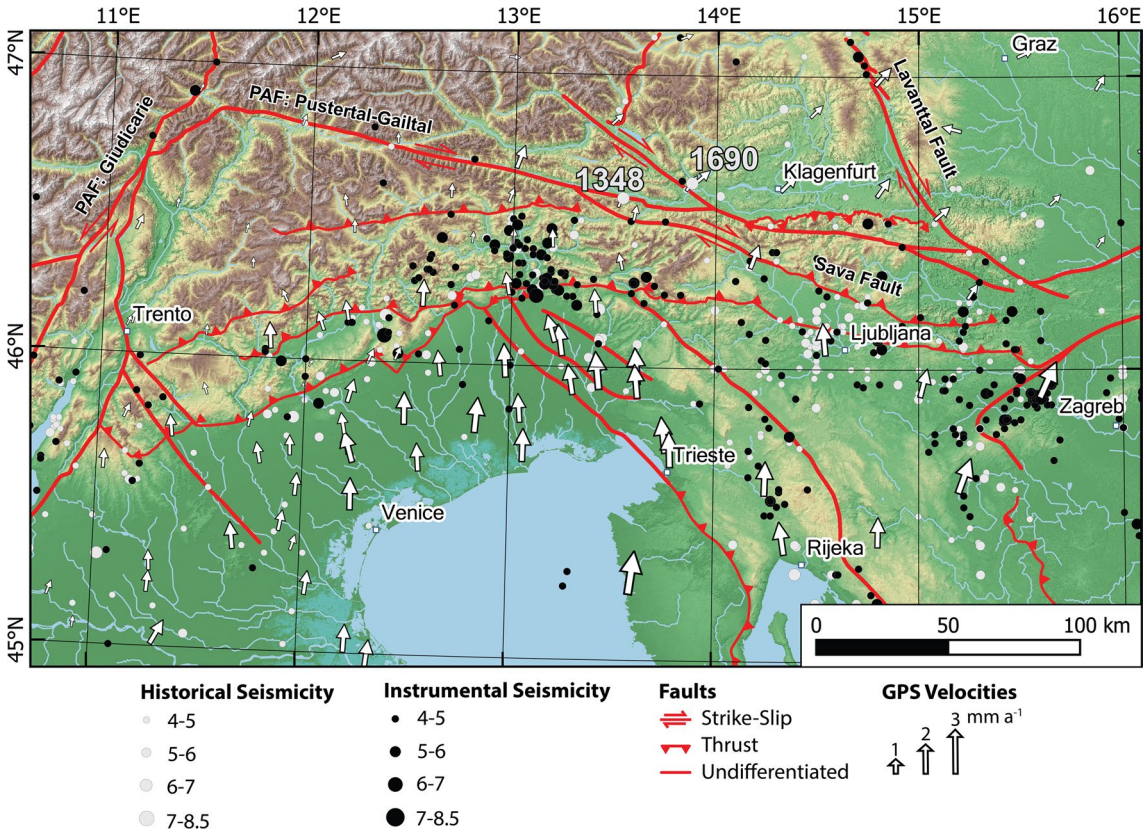

Fig. 3 Historically recorded earthquakes (Grünthal and Wahlström, 2012), instrumentally recorded earthquakes (Stucchi et al. 2012; Jozi Najafabadi et al. 2021; Bagagli et al. 2022), and GPS velocities (D'Agostino et al. 2008; Metois et al. 2015; Serpelloni et al. 2016; Sánchez et al. 2018a, b) in the Eastern and Southern Alps

ESR and OSL for dating active deformation

ESR and OSL dating methods rely on the accumulation of unpaired electrons within traps (i.e., paramagnetic lattice defects) in mineral grains that can be released by different stimuli. These electrons are produced over time by the natural decay of radiogenic nuclides (such as ^{238}U and ^{232}Th, their daughter nuclides, and ^{40}K) and the incidence of cosmic rays. Ikeya et al. (1982) and Miki and Ikeya (1982) studied the potential of ESR to constrain the timing of recent earthquakes in geologic timescales for the first time, using quartz grains from rocks in fault zone cores. Fault gouges are a suitable lithological target for the method because their mineral grains experience frictional heating and grain size comminution directly at the fault core during coseismic slip (Sibson 1977; 1986; Fukuchi 1989). Furthermore, recent experimental studies suggest that the shear heating produced during an earthquake may reset at least partially OSL (Kim et al. 2019; Yang et al. 2019; Oohashi et al. 2020), thermoluminescence (Hiraga et al. 2002; Yang et al. 2019), and ESR (Al center, Yang et al. 2019) signals in fault gouges.

Establishing whether the system was totally or partially reset during a past earthquake event is crucial for determining the significance of the obtained ages. The multiple center and grain-size plateau approaches were developed to aid this assessment. The multiple center approach (Fukuchi 1988) relies on the assumption that discrepancies in the ages obtained for different centers could be the result of uneven reset of the signals during more recent fault movements. Therefore, the agreement between ages obtained from different centers could be considered a criterion for a complete reset of the system during the last seismogenic faulting event along a fault. The grain-size plateau method was proposed by Schwarcz et al. (1987), and further developed and applied in subsequent studies (e.g., Lee & Schwarcz 1994b; Lee 1994). Its basic principle states that after experiencing frictional deformation, grains below a critical radius would become fully reset. Thus, the distribution of ages from different grain size fractions would resemble a plateau ranging from younger ages in smaller particles to older ages in larger ones. The experimental basis for this distribution was initially presented by Buhay et al. (1988) and later expanded

by other authors (Lee and Schwarcz 1993, 1996; Lee 1995). An additional criterion for complete zeroing of the signal during an earthquake was presented by Lee and Schwarcz (1994b), adopting the basic principle behind the multiple center method. This consisted of measuring the distribution from different signals and observing if the youngest ages from at least two plateaus converge, implying that said ages could be interpreted as the time of the last activity of the fault.

ESR dating of quartz has been applied for dating seismotectonic deformation since the 1980s. The studied faults were usually active structures, and the obtained ages indicate at least a partial system reset by fault motion. The earliest applications of ESR to date seismogenic activity using minerals extracted from fault gouges were made in Japan. Ikeya et al. (1982) targeted the Atotsugawa Fault (coseismic slip in 1858; Takeuchi et al. 2003), where they obtained a Pleistocene age of seismogenic faulting (~65 ka) measuring the E' center. Matsumoto et al. (2008) used core samples (389.4 m depth), from the Nojima Fault (1995 Kobe/Great Hanshin Earthquake 6.9 M_w) and observed a decrease in the signal intensity from the Al and E' centers, which was attributed to shear heating partially resetting the signals during earthquakes. Other applications have targeted known active faults outside of Japan such as the San Andreas Fault Zone (San Jacinto segment: Buhay et al. 1988, San Gabriel branch: Lee 1994; Lee and Schwarcz 1996) and the fault zones in the Underground Rock Laboratory in Canada (Lee 1994), which have shown a consistent partial reset of the system.

Only a few studies used OSL for dating seismic slip using minerals from fault gouges. The method has been applied as a geothermometer by Rink et al. (1999) using the sensitization effect of quartz to study the signal resetting related to shear heating during earthquakes. Studies targeting active structures show that the signal has been at least partially reset in fault gouges at the surface and at depth conditions (e.g., Tsakalos et al. 2020). Spencer et al. (2012) studied drill core gouge samples (2604 m depth) from the San Andreas Fault zone, using infrared stimulated luminescence (IRSL) and thermoluminescence signals on poly-mineral and feldspar aliquots. Their dating results (139 ± 12 years) suggest an effective reset of the system by the 7.9 Mw Fort Tejon Earthquake.

Study area and sampling

Suitable sampling localities were scouted using geological maps (Anderle 1977a, b; Bigi et al. 1990a, b; Geološki zavod Slovenije 2003; Rockenschaub & Nowotny 2011; Schuster et al. 2015) and digital elevation models of spatial resolutions ranging from 30 to 1 m (SRTM: NASA JPL 2013; LIDAR ARSO, 2021; KAGIS 2020) from the study area delimited in Fig. 1. In total, three localities along the eastern PAF were studied, with their respective location details reported in Table 1 and the geology summarized in Fig. 4.

The first sampling locality is Mauls in Italy, to the east of the transition between the Giudicarie and the Pustertal–Gailtal segments of the PAF. In the area, the PAF marks the division between high-grade metamorphic Austroalpine units to the north and a tonalite body belonging to the Periadriatic plutons in the south (4384 in Fig. 4b). The sampled outcrop contained gray to greenish cataclastic tonalites within a fault plane oriented 015/55 (nomenclature here and in the following: dip azimuth/dip angle) with slickensides oriented 302/28 (trend/plunge) indicating dextral slip (Fig. 5a). The main fault plane contained ca. 1 m wide, pale gray fault gouge produced by the comminution of the tonalites (Fig. 5b). The second sampled locality is in Finkenstein, Austria. There, the PAF separates the Periadriatic tonalitic lamellae from limestones belonging to the South Alpine units, and it is overlain by potentially displaced Miocene sedimentary units (4427 in Fig. 4b). The sampled outcrop consisted of a body of limestone from the South Alpine units surrounded by blocks of tonalite. At the location, the fault core hosted a dark gray to green fault gouge between tonalites and limestones (Fig. 5c). The third locality is in Plešivec, Slovenia. Here, the PAF placed a tonalitic lamellar body in contact with Triassic limestones from the South Alpine units (4429–4430 in Fig. 4b). In the outcrop, two fault planes hosted a fault gouge within cataclastic tonalites in the vicinity of the contact with the limestones to the south (Fig. 5d, e). The fault planes were oriented 155/73 (Fig. 5e, f), consistent with the regional strike of the PAF

Table 1 Location, altitude, and overburden of the sampled localities

Sample	Locality	Lat.	Long.	Altitude (m)	Overburden (m)
4384	Mauls—Südtirol, Italy	46° 51′ 28.70″ N	11° 32′ 34.40″ E	1133	2
4427	Finkenstein—Carinthia, Austria	46° 32′ 37.92″ N	13° 50′ 47.63″ E	665	2
4429	Plešivec, Slovenia	46° 24′ 36.81″ N	15° 05′ 29.62″ E	487	1.5
4430	Plešivec, Slovenia	46° 24′ 36.18″ N	15° 05′ 29.75″ E	487	1.5

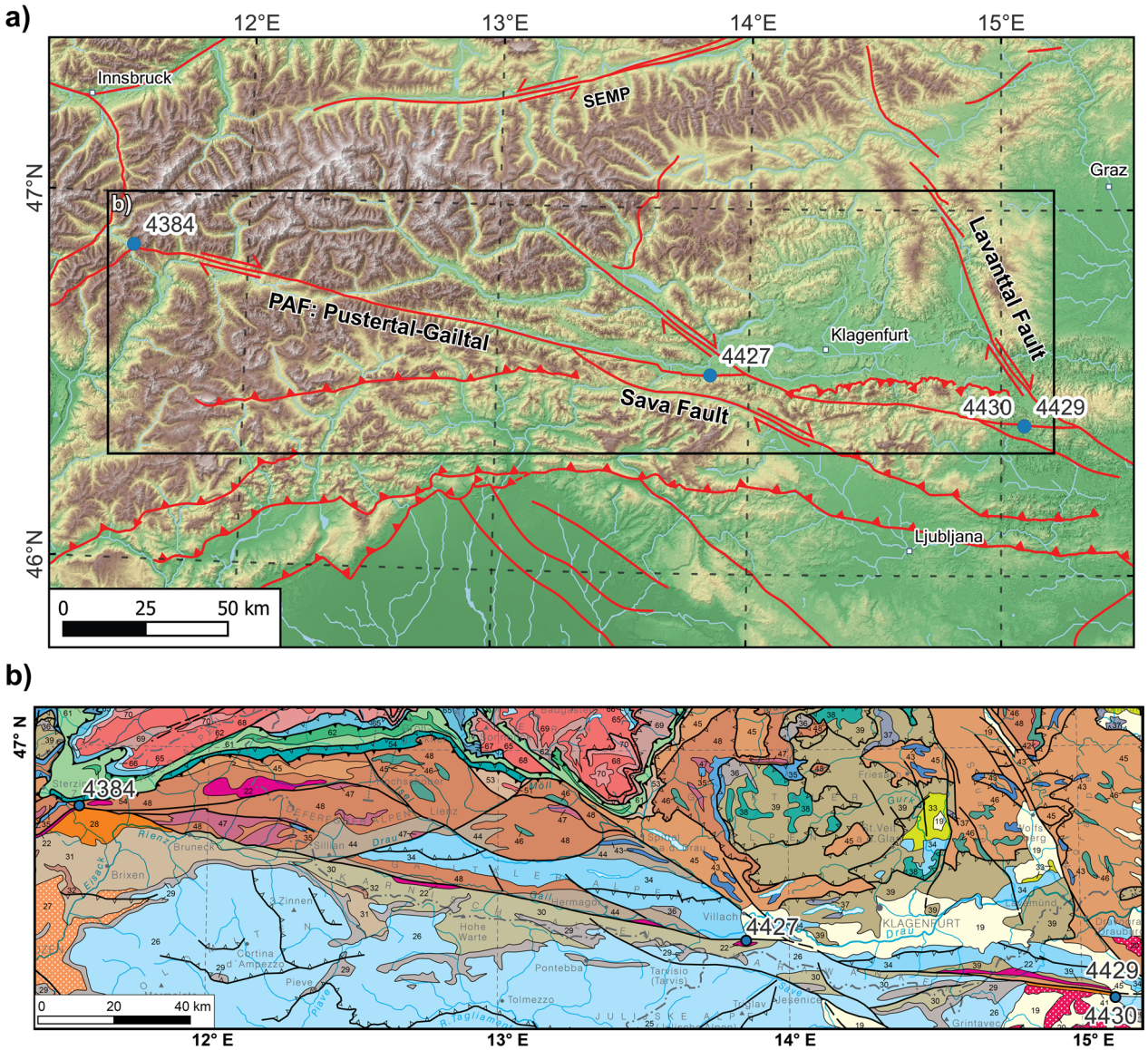

Fig. 4 **a** Sampling localities along the PAF. Fault traces after Schmid et al. (2004). **b** Geological map modified after Schuster et al. (2015), the legend is available in the supplements

at map scale. The gouge exhibited a similarly oriented mm-to-cm-spaced foliation (140/65), forming a compositional layering defined by changes in coloration and possibly mineral components.

To sample the material in the field, we first removed the outermost, weathered portion of the gouge under direct sunlight exposure from each outcrop. Unweathered material was then collected using stainless steel cylinder tubes of 4.2 cm diameter and 15 cm length to avoid sunlight exposition. We collected additional material to determine the natural dose rate via gamma-ray spectrometry. The samples were collected at least 30 cm away from the adjacent wall rock to simplify the assumptions for the dose rate calculation. In cases where the gouges were sampled at a distance below 30 cm from the host rock, a dedicated wall–rock sample was collected to calculate the total dose rate.

Methodology

Sample preparation

All samples were prepared at the facilities of the Leibniz Institute for Applied Geophysics (LIAG)—Hannover, in a dark laboratory under red light conditions to avoid optical bleaching of the signals. The samples were first

Fig. 5 Sampled localities along the PAF. **a** Mauls locality outcrop (sample 4348). **b** Detail of the sampled fault gouge at the Mauls locality outcrop. **c** Finkenstein locality outcrop (sample 4427). **d** Northern section of the Plešivec locality outcrop (sample 4429). **e** Southern section of the Plešivec locality outcrop (sample 4430). **f** Detail of the sampled gouge at the Plešivec locality outcrop showing the foliation in the gouge and the fault plane. **g** Detail of the sampled fault gouge at the Plešivec locality outcrop showing the foliation of the gouge

separated into two grain-size groups by adding water and decanting the finer fraction (< 40 µm) while it was in suspension into a separate container. The coarser portions of the samples (> 40 µm) were dry-sieved and divided into different grain-size ranges. Later, the grain-size fractions between 100 and 250 µm (63–300 µm in cases where the amount of material was considered insufficient) were selected for chemical treatment. Each sample was treated with sodium oxalate (> 24 h, for deflocculation and dissolution of remaining clay aggregates), 30% hydrochloric acid (1–2 h, for carbonate removal), and 30% hydrogen peroxide (> 24 h, for organic material removal). The resulting material was then separated into groups of mineral phases using heavy liquid solutions of Na-polytungstate with densities between 2.62 g/cm^3 and 2.7 g/cm^3 for quartz and below 2.58 g/cm^3 for K-feldspar. Afterward, the fraction corresponding to quartz was etched using 40% hydrofluoric acid for 1 h, and any resulting fluoride precipitates were removed with 20% hydrochloric acid. Finally, the resulting quartz and the fraction corresponding to potassium feldspar were sieved separately into three grain-size ranges corresponding to 100–150 µm, 150–200 µm, and 200–250 µm.

Gamma-ray spectrometry sample preparation and dose rate measurements

The samples used to obtain the natural dose rates were collected simultaneously with the ESR/OSL samples from the same sampled spots within the fault gouge outcrops. These samples were prepared and measured at the facilities of LIAG. The initial material was dried at 110 °C for 24 h to obtain the natural water content by comparing the weight of the samples before and after drying. We assumed a 5% error in the natural water content. Due to the high amount of clay minerals in the samples, the material was aggregated after drying. Therefore, the samples were deconsolidated using a jaw crusher with an aperture of around 1–3 mm. Finally, 700 g of the resulting material was deposited in a sealed plastic container for 4 weeks to ensure equilibrium between ^{222}Rn and its daughter nuclides.

An estimation of the radionuclide concentrations (^{238}U, ^{232}Th, and ^{40}K) was obtained by measuring the samples with an Ortec N-type HPGe gamma spectrometer. The dose rates for quartz and feldspar were calculated using the compositions and the conversion factors from Liritzis et al. (2012), the alpha attenuation factor calculation after Brennan (1991), the beta absorption factors from Guerin et al. (2012), the etching factor for beta absorption from Brennan (2003), the absorbed dose fraction of Rb from Readhead (2002), and the cosmic ray calculation from Prescott & Hutton (1994). We assumed no Rn loss and an etching depth for quartz of 10 µm. For feldspar, we calculated the internal dose rates using a K content of 12.5 ± 1.0% after Huntley and Baril (1997). For sample 4427, the distance between the gouge sample and the wall rock was 25 cm. Therefore, the gamma dose rate of the sample was calculated using the scaling factor following Aitken (1985).

ESR measuring parameters and protocols

The ESR measurements were conducted using an X-band JEOL FA100 series spectrometer. The aliquots consisted of 60 mg quartz in the grain size range of 100–150 µm contained in quartz glass tubes of 2 mm inner diameter. During the measurements, the microwave power was set to 10 mW using a 100 kHz modulation, with magnetic sweeps of 1 min and a sweep width of 30 mT. We measured the spectra under temperatures of − 160 °C and − 156.5 °C. The intensities from the Al center (Fig. 6) were calculated from the first positive peak (g ~ 2.02) to the last negative peak of the spectra (g ~ 1.99) and were then normalized using the 6th line of the Mn marker (g ~ 1.88), permanently inserted in the cavity. The Ti center could also be observed under the same conditions, but it was not recorded due to a very weak intensity in the analyzed samples. To account for the crystallographic anisotropy of quartz, each aliquot was measured three times, manually rotating the sample tube by 60° before recording the spectra. A mean intensity was calculated from these three measurements of the Al center and the uncertainty was estimated as ± 1σ standard error.

A custom-built external X-ray radiation machine (Oppermann and Tsukamoto 2015) was used to irradiate, preheat, and thermally reset the signals in the aliquots. The X-ray tube provides a dose rate of 0.302 ± 0.014 Gy/s

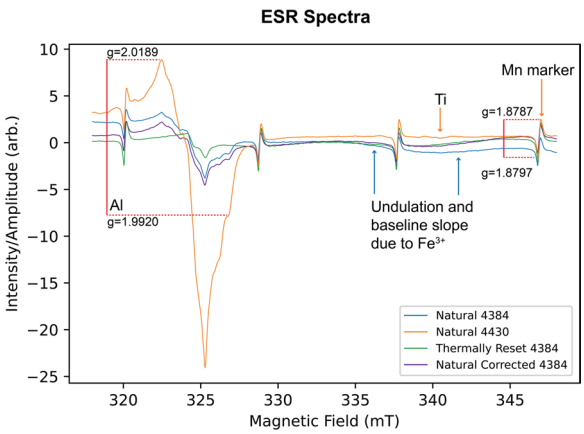

Fig. 6 ESR spectra indicating the position of the Al and Ti centers, the Mn marker, and peaks used for the calculation of the intensities. The spectra examples include measurements from a natural aliquot, a thermally reset aliquot, the undulated pattern produced by the Fe contamination, and the results of the baseline correction

with a mean energy of 26 keV (Tsukamoto et al. 2021). Following the SAR protocol (Table 2a, left) established by Tsukamoto et al. (2015), all aliquots were preheated at 160 °C for 4 min (preheating conditions test explained in "Preheat test"Sect.) after each laboratory irradiation to eliminate the thermally unstable portion of the signal.

We heated the aliquots to a temperature of 420 °C for 4 min before administering regenerative doses, following the procedure after Tsukamoto et al. (2015), which indicates that at these conditions the signal from the Al center can be effectively removed (green spectrum in Fig. 6). Measurements applying the SAAD protocol (Table 2a, right) were conducted to verify the validity of the applied SAR protocol. Detailed explanations of the applied protocols and the quality controls used for ESR are provided in the following sections. For both applied protocols, a single aliquot from each sample was used to obtain an equivalent dose (D_e) value.

SAR protocol

For this protocol, we first preheated and measured a natural intensity in a single aliquot of the sample. Then, the aliquot was thermally reset and measured to record the zero-dose intensity. A dose response curve (DRC) was then constructed by measuring the intensities after increasing irradiation steps (at around 300 Gy, 900 Gy, 2700 Gy, 5100 Gy, 7500 Gy, and 10,600 Gy) until the saturation intensity was reached (i.e., the intensity at which the addition of further laboratory dose increments does not yield a stronger signal) and subtracting the zero-dose intensity (including the overlapping Peroxy center) from each measurement. The data points were fitted to a single saturating exponential function (Eq. 1), where I_{sat} (a. u.) is the saturation intensity and D_0 describes the characteristic saturation dose in Gy. The D_e (Gy) was obtained by projecting the natural intensity onto the DRC (Fig. 7a). The uncertainty of the D_e was obtained from the median absolute deviation of the distribution resulting from a Monte-Carlo simulation of 2000 repetitions to fit the curve to randomized data points within the standard error of the measurements:

$$I(D) = I_{sat}(1 - e^{\frac{-D}{D_0}}) \quad (1)$$

SAAD protocol

This protocol relies on the extrapolation of a DRC built starting from the natural intensity and with measurements recorded after subsequent steps of increasing irradiation (starting at around 600 Gy, then 1800 Gy, 4200 Gy, 6600 Gy, 9600 Gy, up to 12,700 Gy) on the same aliquot (Fig. 7b). The zero-dose intensity (obtained from

Table 2 a) Description of the applied ESR SAR and SAAD protocols

(a) ESR SAR and SAAD protocol

Step	Treatment SAR	Treatment SAAD
1	Preheat at 160 °C for 240 s	Preheat at 160 °C for 240 s
2	Natural ESR measurement	Natural ESR measurement
3	Thermal reset at 420 °C for 240 s	Additive dose irradiation
4	Zero-dose ESR measurement	Preheat at 160 °C for 240 s
5	Dose irradiation	Added dose ESR measurement
6	Preheat at 160 °C for 240 s	Repeat 3–5
7	Regenerated ESR measurement	
8	Repeat 5–7	

(b) Post-IR IRSL SAR protocol

Step	Treatment	Measurement
1	Dose irradiation	
2	Preheat at 250 °C for 60 s	
3	IRSL at 50 °C for 100 s	L_{x50}
4	IRSL at 225 °C for 200 s	L_{x225}
5	Test dose	
6	Preheat at 250 °C for 60 s	
7	IRSL at 50 °C for 100 s	T_{x50}
8	IRSL at 225 °C for 200 s	T_{x225}
9	Repeat 1–8	

(b) Description of the protocol used to measure the $pIRIR_{225}$ and IR_{50} OSL signals in potassium feldspar. No dose was given to the natural signals

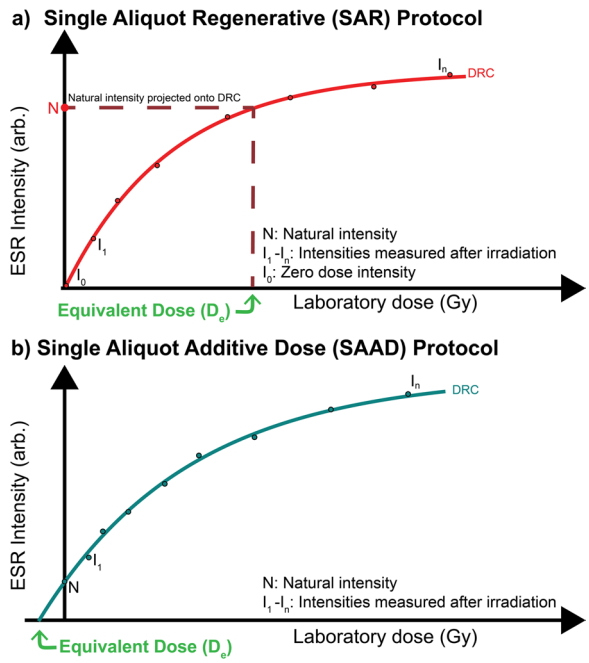

Fig. 7 Estimation of the D_e for: **a** SAR protocol. **b** SAAD protocol. Modified after Tsukamoto et al. (2020)

the SAR protocol) was subtracted from each measurement, and the dose–response curve was constructed by fitting the obtained data points to a single saturated exponential function (Eq. 2), where I_{sat} (a. u.) is the saturation intensity, D_e is the equivalent dose in Gy, and D_0 is the characteristic saturation dose in Gy. The uncertainty of the D_e was obtained from the median absolute deviation of the distribution resulting from a Monte-Carlo simulation of 2000 repetitions. For each iteration of the simulation, a DRC was fit to randomized data points within the standard error of the measurements and a single D_e was obtained from the x-intercept (extrapolation) of the curve:

$$I(D) = I_{sat}(1 - e^{\frac{-D+D_e}{D_0}}) \quad (2)$$

Preheat test

A preheat test was conducted to verify the temperature necessary to remove the thermally unstable part of the signal introduced after laboratory irradiation. In this case, a natural and a laboratory-irradiated (thermally reset, then irradiated to ~ 3000 Gy) aliquot from the same sample were selected. The Al center intensity of each aliquot was initially measured without preheating (room temperature preheat). Then, the intensity was measured after heating steps of 4 min at temperatures of 100 °C, 130 °C, 160 °C, 190 °C, 220 °C, and 250 °C. For both aliquots, the intensity from the Al center was compared to the respective preheating temperature of the step to obtain the curves displayed in Fig. 8a. The plateau shows that the Al center intensity for the natural aliquot starts decaying at preheating temperatures larger than 190 °C. On the other hand, there are two-step decays for the laboratory-irradiated aliquot. The first one starts after preheating at 100 °C where the thermally unstable portion of the signal starts to be evicted, and the second one occurs above 160 °C where partial resetting of the signal starts. The comparison of the laboratory-irradiated and the natural aliquot in Fig. 8a shows that the intensities at the 160 °C preheating temperature are comparable between both aliquots. Moreover, the anomalous

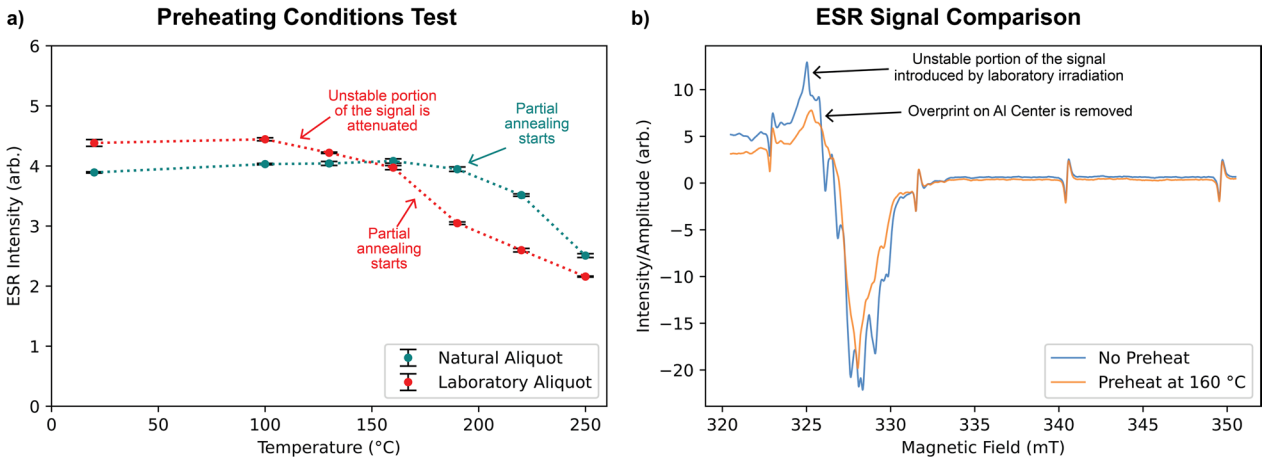

Fig. 8 Preheating conditions test for a natural and a regenerated aliquot from one of the Plešivec locality samples (4430). **a** Preheating plateau test for a naturally irradiated aliquot and a thermally reset and subsequently irradiated aliquot. **b** Comparison of the spectra before and after preheating at 160 °C for the regenerated aliquot

peak introduced by laboratory irradiation is effectively removed after preheating at 160 °C (Fig. 8b), which confirms it as the optimal preheat temperature (Additional file 1: Figure S1, Additional file 2: Figure S1).

Isothermal decay test

Thermally assisted escape of the electrons from the traps can result in signal loss, and therefore, it may lead to an age underestimation. An isothermal decay test helps to assess how significant is the effect of thermal de-trapping. We conducted a test based on the study by Toyoda and Ikeya (1991) by selecting four aliquots from the same sample, each corresponding to a different isothermal holding temperature (160 °C, 190 °C, 220 °C, and 250 °C). The aliquots were thermally reset at 420 °C for 4 min, irradiated to a dose of around 5000 Gy, then preheated at 160 °C for 4 min (according to the results of the preheating conditions test) to normalize all signal intensities, and measured to record the corresponding initial intensity of the Al center. Successive steps of heating and measuring were conducted, maintaining the respective isothermal heating temperature for each aliquot but doubling the heating time from the previous iteration, starting at 4 min until reaching a heating time of about 2 h.

After the measurements were completed, each intensity was normalized to the initial irradiated intensity from the respective aliquot recorded after the preheating step. We calculated the kinetic parameters using the ESR MATLAB toolboxes after King et al. (2020). The thermal lifetime (τ_{th}) was obtained using the Gaussian model after Lambert (2018) described by the convolution integral in Eq. 3, where $P_{(E_a)}$ (Eq. 4) and $\tau_{(E_t)}$ (Eq. 5) are the probability of electrons escaping from the trap due to thermal effects (a. u.) and the corresponding thermal lifetime in seconds at a specific trap depth (E_t), respectively. $\sigma(E_t)$ is the Gaussian distribution of activation energies in eV around the mean trap depth $\mu(E_t)$ in eV, s is the frequency factor in s^{-1}, k_B is the Boltzmann constant in eV^*K^{-1}, and T is the ambient temperature in K:

$$\tau_{th} = \int_0^{E_t max} P_{(E_t)} * \tau_{(E_t)} dE_t \tag{3}$$

$$P_{(E_t)} = \frac{1}{\sigma(E_t)\sqrt{2\pi}} e^{\left[\frac{1}{-2}\left[\frac{E_t-\mu(E_t)}{\sigma(E_t)}\right]^2\right]} \tag{4}$$

$$\tau_{(E_t)} = s^{-1} e^{\frac{E_t}{K_B * T}} \tag{5}$$

Dose recovery test

We conducted a dose recovery test to confirm whether the thermal reset step in the SAR protocol induces a sensitivity change. Beerten et al. (2008) originally introduced a dose recovery test using quartz for ESR dating. However, they heated the sample at 500 °C for 1 h before a dose was given, and its effectiveness in monitoring any sensitivity change on natural aliquots in the SAR protocol was unclear. Tsukamoto et al. (2017) proposed a dose recovery test using modern sediment samples, and a similar approach was applied in subsequent studies (Richter and Tsukamoto 2022; Richter et al. 2022). In this study, we followed a modified procedure proposed by Toyoda et al. (2009), which is a regenerative-additive method and has been demonstrated as a means for conducting the dose recovery test by Fang and Grün (2020) and Richter et al. (2022). For this, the intensities measured using the SAAD protocol were compared to the calculated DRC from the SAR protocol. Apparent D_e values were calculated by projecting the SAAD intensities onto the SAR curve. The obtained D_e values were then compared to the added dose from each SAAD protocol measurement following the regenerative-additive dose plot. The slope of this plot is equivalent to the dose recovery ratio, and if this is close to unity (slope is 1), the SAR protocol is regarded to be robust. However, unlike the dose recovery test in luminescence dating, in which the dose recovery test is conducted using laboratory-bleached aliquots, it is difficult to reset the quartz ESR signals without heating the aliquots before a given dose is administered. Therefore, the dose recovery test may be affected by the signal saturation (i.e., the slope may not be linear) Additional file 3: Table S1, Additional file 4: Table S2).

OSL equipment, protocol, and data processing

For OSL, we used K-feldspar aliquots with a diameter of 2 mm and material in the grain size fraction of 100–150 µm, mounted on stainless steel disks with a diameter of 9.80 mm. The measurements were recorded with a Risø TL/OSL DA-20 reader available in the facilities of LIAG—Hannover. The reader is equipped with a beta $^{90}Sr/^{90}Y$ source that provides a dose rate of 0.119 ± 0.006 Gy/s. For stimulation, the reader includes LEDs emitting infrared (870 ± 40 nm, 3 clusters of 7 LEDs with a total maximum power of 145 mW/cm^2). The light detection system of the reader includes a photomultiplier tube (bialkali EMI 9235QB) with a maximum detection efficiency between 200 and 400 nm and blue detection filters (Schött BG-39 and Corning 7–59) with a transmission window in the blue–violet region between 320 and 450 nm. We used IR optical stimulation at 90% power, and in cases where the light level was too bright for the detector, an extra neutral density filter (ND 1.0). For acquisition and initial processing, we used the Risø software suite. The R luminescence package after Kreutzer

et al. (2012) was used to calculate the fading rate and corrected ages.

SAR protocol

We measured the IR_{50} signal after Thomsen et al. (2008) and the $pIRIR_{225}$ signal after Buylaert et al. (2009), applying a SAR protocol summarized in Table 2b. The first step of the procedure consisted of preheating the aliquots at a temperature of 250 °C for 60 s. Next, the measurements were conducted during a first IR stimulation for 100 s at 50 °C, followed by a second IR stimulation for 200 s at °C. Five aliquots from each sample were measured to obtain a mean natural intensity with the uncertainty calculated using the standard error of the measurements. Three of these aliquots were selected for measurements to build the DRCs. The aliquots were separately measured after giving doses of approximately 0 Gy, 110 Gy, 220 Gy, 560 Gy, 1130 Gy, and 2260 Gy, with a test dose of 90 Gy. The IR_{50} intensities were calculated using the first 5 s of stimulation for the signal and the last 10 s for the background. The $pIRIR_{225}$ intensities were calculated using the first 10 s of stimulation for the signal and the last 20 s for the background.

The acceptance of the measurements was evaluated using two criteria after Murray and Wintle (2000). The first is the recycling ratio, which was calculated by dividing the sensitivity-corrected intensity of the recycling dose measurement by the corresponding intensity obtained at the same dose value during the dose–response curve measurement run. An acceptable recycling ratio should be close to 1, with a margin of error of 10%. The second is the recuperation rate, which was obtained by dividing the sensitivity-corrected intensity of the zero-dose measurement by the sensitivity-corrected natural intensity. The recuperation rate should not exceed 5%.

The dose–response curves were constructed by fitting the data from at least three measured aliquots from each sample to a single saturating exponential function (Eq. 6), where I_{sat} is the saturation intensity (a. u.) and D_0 is the characteristic saturation dose in Gy. A fading test was performed using three bleached aliquots from each sample that were irradiated to a dose of around 240 Gy. Then, the signals were measured at different time intervals after the irradiation steps. The fading test data were processed using the R Luminescence package after Kreutzer et al. (2012) to calculate the g value and recombination center density ("analyse_FadingMeasurement" function) after the model from Huntley (2006) and to apply the fading correction ("calc_Huntley2006" function) after Kars et al. (2008), modeling the natural simulated DRCs and correcting the D_e. Saturation levels were estimated by dividing the natural intensity by the saturation intensity of the fading-corrected DRC:

$$I(D) = I_{sat}(1 - e^{\frac{-D+c}{D_0}}) \quad (6)$$

The reliability of the applied protocols was confirmed by implementing a dose recovery test conducted using six aliquots from each sample. The aliquots were bleached for 4 h using a Hönle UVACUBE 400 solar simulator. To test the dose recovery ratio, half of the bleached aliquots were then given a known dose which was subsequently measured using their respective DRC. A residual dose was obtained by comparing the remaining dose after bleaching to DRCs measured from the other half of the aliquots. Finally, the dose recovery ratio was calculated by subtracting the residual dose from the irradiated D_e and then dividing the value by the irradiated dose.

Age calculation

We calculated the ages following the standard procedure in trapped charge dating. Each D_e was divided by the respective dose rates for feldspar in OSL and for quartz in ESR. The uncertainty of the ages was calculated by propagating the error from the dose rate and the D_e. We calculated a minimum age using the double of the characteristic saturation dose ($2D_0$) instead of the D_e for the samples that could be considered in saturation (i.e., saturation level > 86% or $D_e > 2D_0$).

Results

Dose rates

The calculated dose rates for feldspar fall between 1.92 ± 0.12 and 4.72 ± 0.21 Gy/ka, and for quartz between 1.34 ± 0.06 and 3.99 ± 0.18 Gy/ka. Since the dose rates calculated for feldspar depend on the internal K content and the external alpha value, they are generally larger than the ones calculated for quartz. However, the low alpha content indicates that in this case, the dose rates are more influenced by the internal K content. The complete list of the results, including the respective contents of radiogenic nuclides, water, and contribution by cosmic rays, is reported in Table 3. The dose rates from the Mauls and Finkenstein localities are overall lower than the ones in the Plešivec locality samples. This is most likely due to differences in mineralogy between the gouges associated with the lithologies involved in comminution.

ESR dating

A strong signal from the Al center was detected in the measured ESR spectra of the samples, usually accompanied by a very weak signal from the Ti center (orange spectrum in Fig. 6). Due to this effect, the measurements were recorded only from the Al center. The aliquots from

Table 3 Radiogenic nuclide compositions, water content, and calculated dose rates for the fault gouge samples

Sample	K (%)	Th (ppm)	U (ppm)	Water content (%)	Cosmogenic Dose Rate (Gy/ka)	Ext. Alpha Kfs	Dose rate Kfs (Gy/ka)	Dose rate Qtz (Gy/ka)
4384–Mauls	0.74 ± 0.03	3.66 ± 0.18	0.94 ± 0.05	7 ± 5	0.20 ± 0.02	0.06 ± 0.02	1.92 ± 0.12	1.34 ± 0.06
4427—Finkenstein	1.65 ± 0.08	11.33 ± 0.57	2.26 ± 0.11	39 ± 5	0.16 ± 0.02	0.11 ± 0.02	2.86 ± 0.13	2.21 ± 0.08
4427 (Wall rock)—Finkenstein	0.11 ± 0.05	0.58 ± 0.02	0.45 ± 0.04	0	0.16 ± 0.02	0.01 ± 0.00	0.96 ± 0.11	0.42 ± 0.02
4427 (Total)—Finkenstein	–	–	–	–	0.16 ± 0.02	–	2.79 ± 0.17	2.14 ± 0.08
4429—Plešivec	2.45 ± 0.12	12.86 ± 0.64	3.17 ± 0.16	14 ± 5	0.16 ± 0.02	0.18 ± 0.04	4.44 ± 0.20	3.72 ± 0.17
4430—Plešivec	2.68 ± 0.13	14.25 ± 0.71	2.88 ± 0.14	13 ± 5	0.16 ± 0.02	0.19 ± 0.04	4.72 ± 0.21	3.99 ± 0.18

the Mauls sample (4384) presented a subtle Fe^{3+} contamination, observed as a long-wavelength undulation superimposed on the spectra and a slight negative baseline slope (blue spectrum in Fig. 6). However, the effect of the overprint was not strong enough to completely mask the signal of the Al center, meaning that the intensity could still be calculated. An additional baseline correction was performed on the spectra measured from this sample using the cwESR processing software (purple spectrum in Fig. 6).

The dose–response curves of the measured aliquots from each locality using the SAR and SAAD protocols are presented in Fig. 9, with the respective fit parameters available in the supplementary material. Most of the SAAD protocol DRC had a considerable amount of extrapolation to obtain the D_e, and there is a large uncertainty in the fit of the curve in the extrapolated portions. Overall, the D_e obtained using the SAAD protocol are larger than the ones obtained with the SAR protocol. For the latter, all D_e belong to measurements with intensities below the saturation points of the DRCs. The D_e obtained using the SAR protocol range between 1232 ± 23 Gy and 3026 ± 47 Gy, while for the SAAD protocol, they range between 1871 ± 55 Gy and 3426 ± 239 Gy. The difference in D_e values between the measurements from both protocols is carried over to the calculated ages. The SAR protocol ages range from 552 ± 26 to 1075 ± 47 ka, while the ages obtained with the SAAD protocol span from 530 ± 33 to 1522 ± 73 ka. A complete overview of the calculated D_e values, their respective ages using both protocols, and the saturation level of the natural intensity is presented in Table 4.

The applied ESR dose recovery test shows that the relationship between the apparent D_e and the added dose is sample-dependent. The Mauls (4384, Fig. 10a) and Finkenstein (4427, Fig. 10b) samples present a good correlation with dose recovery ratios of 0.88 ± 0.04 and 1.07 ± 0.23, respectively. However, for the Finkenstein sample, the uncertainty of the linear fit is large. Both Plešivec locality samples present a lower correlation, with dose recovery ratios of 0.64 ± 0.09 (sample 4429; Fig. 10c) and 0.78 ± 0.08 (sample 4430; Fig. 10d). Changes in sensitivity between the protocols can also be evaluated by shifting the SAAD curves by the respective SAR D_e and comparing them to the SAR DRCs (Fig. 11). For the studied samples, the shifted SAAD curves present an overall good match to the SAR measurements and curves, and most of the differences lie in the extrapolated portions of each SAAD DRC.

The results from the isothermal decay test performed using aliquots from sample 4430 (Plešivec locality) are presented in Fig. 12. From the fit to the Gaussian model, we obtained an activation energy of 1.20 ± 0.08 eV, a distribution around the trap depth $\sigma(E_t)$ of 0.16 ± 0.01 eV, and a frequency factor of $10^{9.09\pm0.88}$ s^{-1}. Using these values and assuming an environmental temperature of 10 °C, the calculated lifetime of the Al center is 4.20*10^7 Ma.

OSL dating

The IR_{50} and $pIRIR_{225}$ signals were measured for the samples obtained from Mauls (sample 4384 in Fig. 13a) and Plešivec (samples 4429 and 4430 in Fig. 13b, c, respectively). The sample from the Finkenstein locality (4427) could not be measured due to the absence of potassium feldspar in the fault gouge. After correcting the laboratory DRCs for anomalous fading, the samples show either a saturated state (i.e., $D_e > 2D_0$ or saturation level > 86%) or are very close to saturation. The respective DRC before and after accounting for anomalous fading are displayed in Fig. 13. According to the saturation levels presented in Table 5, all the $pIRIR_{225}$ signal measurements indicate saturation, whereas for the IR_{50} signal the level is below but close to the threshold value. The effect of anomalous fading is more drastic for the IR_{50} signal because of the larger g values (3.43 ± 0.31–3.48 ± 0.37%/decade) compared to those of the $pIRIR_{225}$ signal (1.97 ± 0.36–2.24 ± 0.34%/

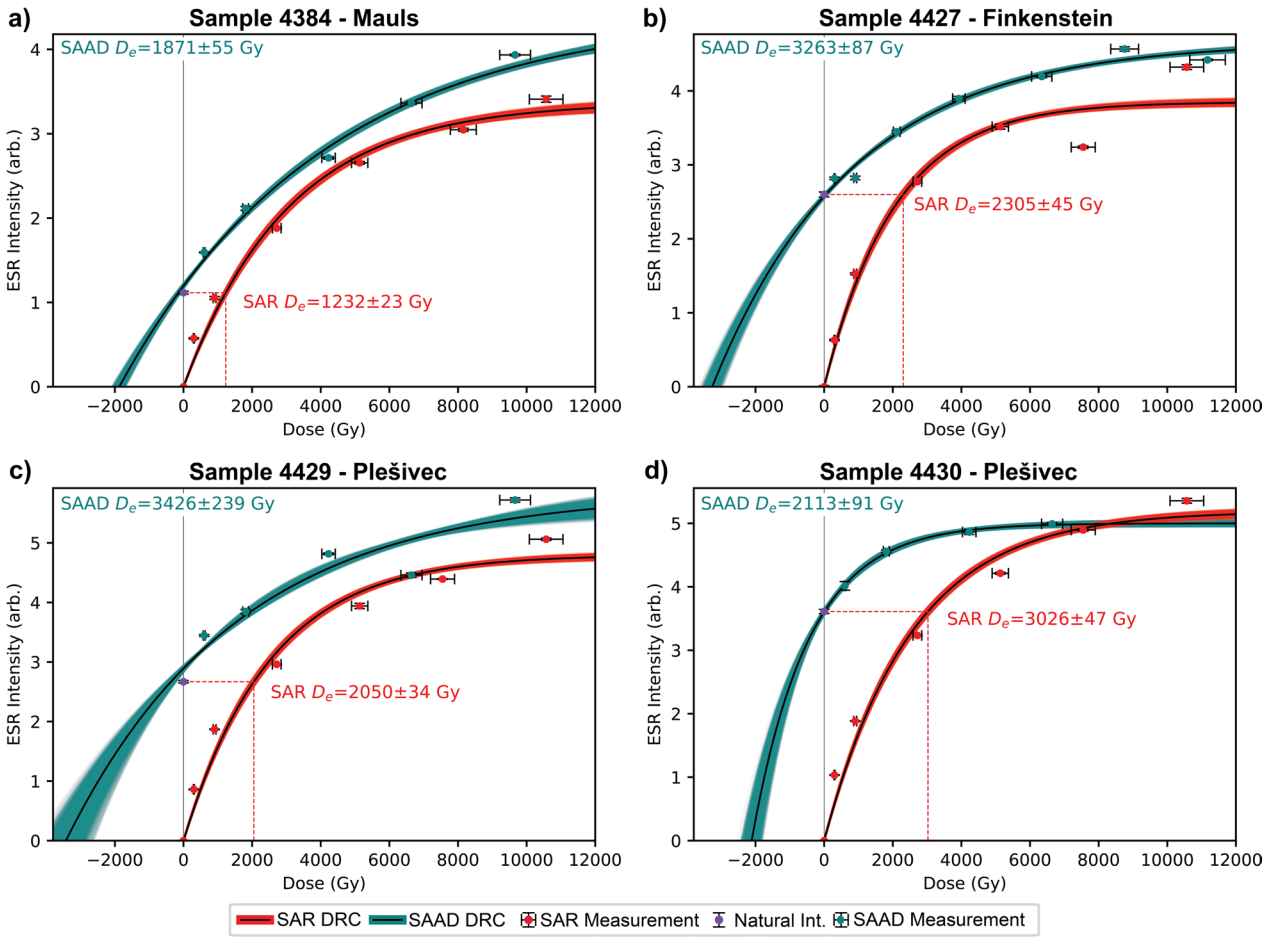

Fig. 9 ESR dose–response curves for the Al center obtained with the SAR and SAAD ESR protocols for the samples: **a** 4384—Mauls locality. **b** 4427—Finkenstein locality. **c** 4429—Plešivec locality. **d** 4430—Plešivec locality. The colored area surrounding the respective best fit of the dose response curve contains the curves fitted in 2000 simulations

Table 4 Results from ESR dating measuring the SAAD and SAR protocols on quartz aliquots

Sample	Saturation Level (%)		D_e (Gy)		Age (ky)	
	ESR SAR	ESR SAAD	ESR SAR	ESR SAAD	ESR SAR	ESR SAAD
4384–Mauls	33.1 ± 1.8	25.1 ± 1.5	1232 ± 23	1871 ± 55	922 ± 44	1400 ± 75
4427–Finkenstein	67.5 ± 4.5	55.8 ± 2.2	2305 ± 45	3263 ± 87	1075 ± 47	1522 ± 73
4429–Plešivec	55.6 ± 3.3	45.6 ± 9.6	2050 ± 34	3426 ± 239	552 ± 26	922 ± 76
4430–Plešivec	69.6 ± 3.8	72.2 ± 0.8	3026 ± 47	2113 ± 91	759 ± 36	530 ± 33

decade). The obtained D_e values from both signals and the respective $2D_0$ values from the DRCs are reported in Table 5. The complete list of parameters of the DRCs before and after correcting for fading with the respective ρ' and g values used for the correction is available in the supplementary material.

Due to the saturation of the $pIRIR_{225}$ signal, we calculated minimum ages using the $2D_0$ instead of the D_e. For the IR_{50} signal, the combination of a near saturated state and a larger fading correction factor of the signal (g value) implies a less reliable D_e estimation. Therefore, minimum ages were also calculated using $2D_0$ instead of the D_e. The obtained ages are reported in the respective columns of Table 5. For the Mauls sample (4384), the difference between the $2D_0$ values in both measured signals results in a large minimum age

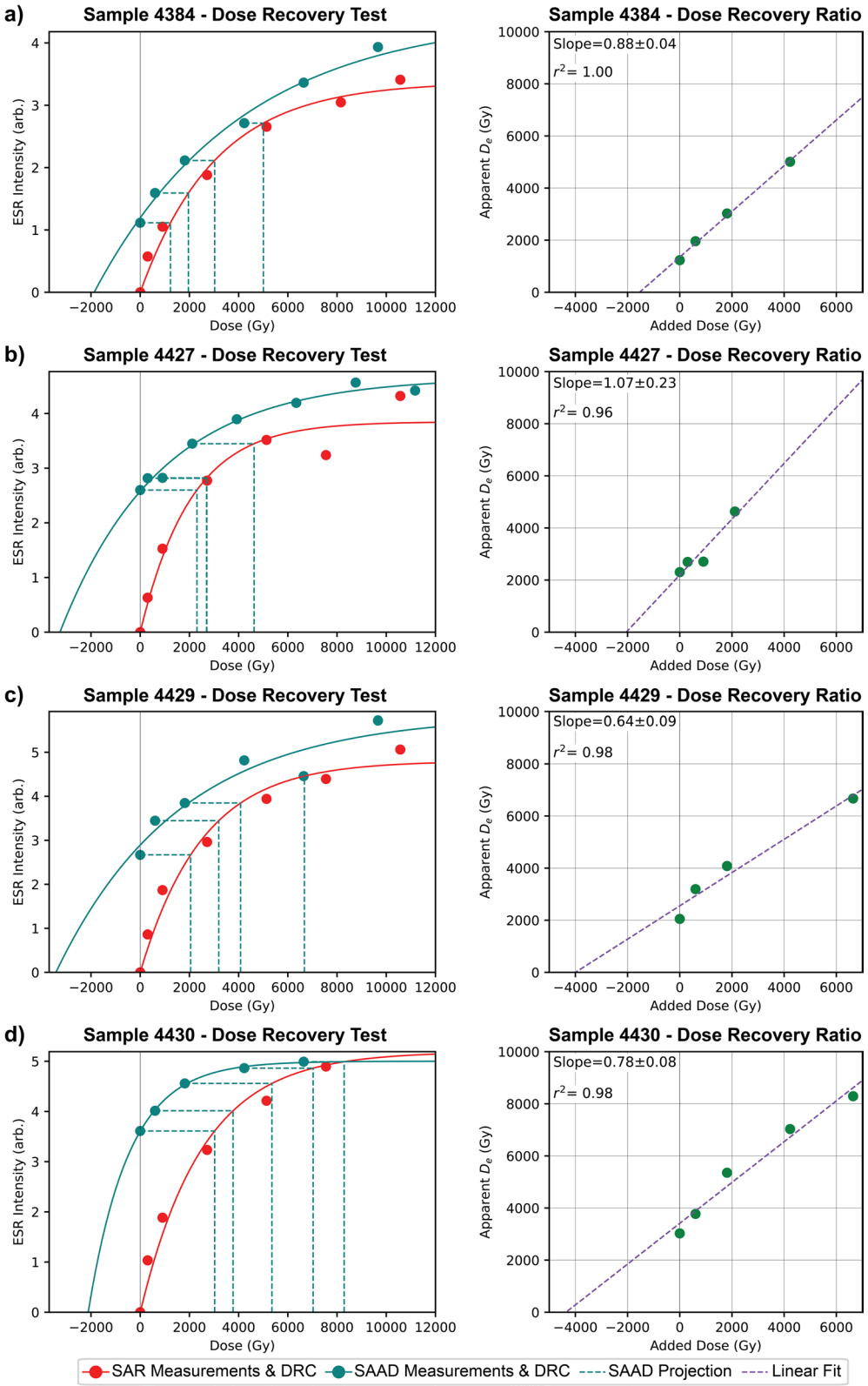

Fig. 10 Dose recovery test for ESR dating. Projection of the SAAD measurements onto the SAR dose response curves (left) and comparison of the apparent SAAD D_e and SAAD added doses (right) for the samples: **a** 4384—Mauls locality. **b** 4427—Finkenstein locality. **c** 4429—Plešivec locality. **d** 4430—Plešivec locality

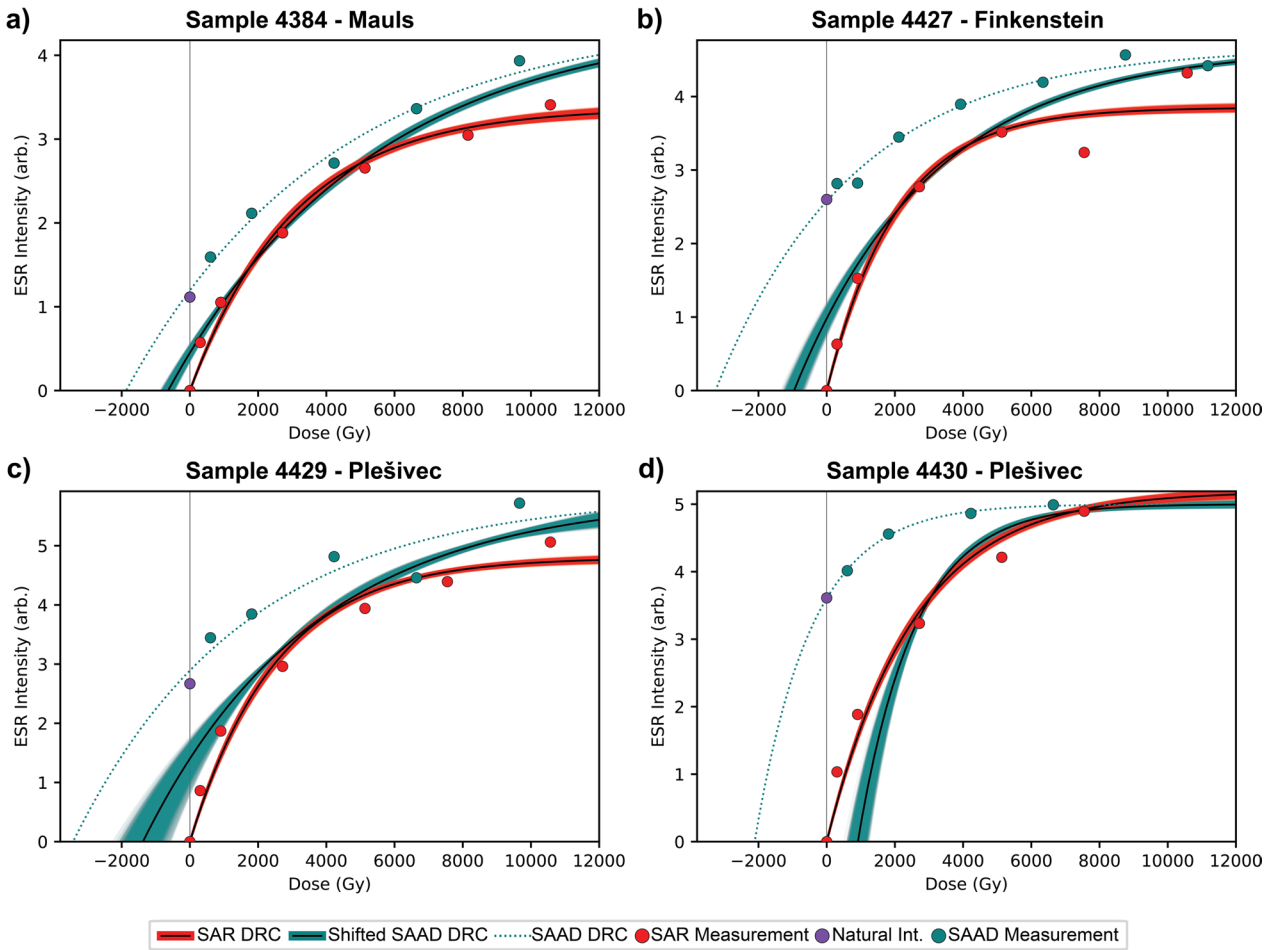

Fig. 11 SAAD protocol dose response curves shifted by their respective SAR protocol D_e for the samples: **a** 4384—Mauls locality. **b** 4427—Finkenstein locality. **c** 4429—Plešivec locality. **d** 4430—Plešivec locality

variation, where from the $pIRIR_{225}$ signal the calculated age is 196 ± 12 ka and approximately 335 ± 21 ka from the IR_{50} signal. The ages from both signals for the two Plešivec samples fall within the margin of error of each other. For sample 4429, the ages are 281 ± 16 ka and 279 ± 13 ka for the $pIRIR_{225}$ signal and the IR_{50} signal, respectively, while for sample 4430, the ages are 280 ± 13 ka for the $pIRIR_{225}$ signal and 295 ± 13 ka for the IR_{50} signal.

The dose recovery ratio was calculated with and without the subtraction of the residual dose and presented in Table 5. The results of the dose recovery test present little variation before and after subtracting the residual, and the values indicate an overall good quality of the measurements, with recovery ratios larger than 85% for both signals.

Discussion

In general, the equivalent doses and ESR ages (Table 4) obtained with the SAAD and SAR protocols are not in agreement. The SAAD DRCs in Fig. 9 involve a large extrapolation that introduces more uncertainty at the time of the D_e calculation, especially when dealing with older samples that present natural intensities closer to the saturation point of the curve. This results in SAAD ages that, when compared to their SAR counterparts, are older and have a larger uncertainty. The main advantage of the SAR protocol over the SAAD protocol is that for the SAR protocol, it is not necessary to extrapolate a large portion of the DRC to obtain the D_e. Despite the difficulty in accounting for sensitivity changes during the thermal reset step when applying the SAR protocol, our results from the dose recovery in Fig. 10 test show dose

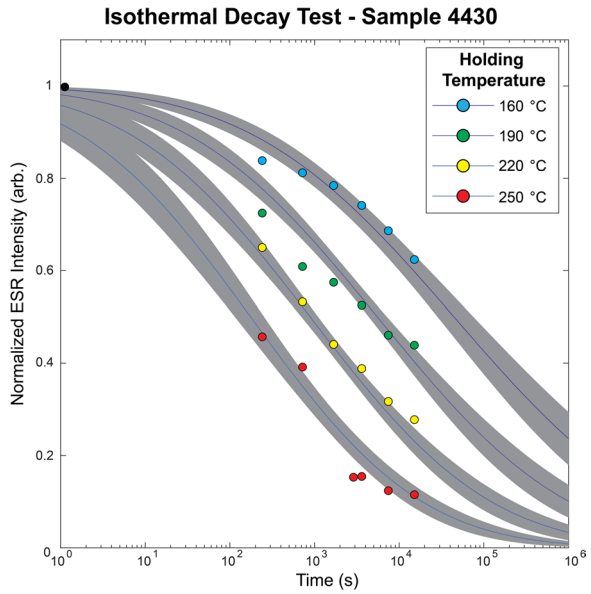

Fig. 12 ESR isothermal decay test performed on an aliquot from the Plešivec locality (sample 4430) at four different holding temperatures

recovery rates close to unity and indicate that the curves are comparable to those of the SAAD protocol (Fig. 11). Therefore, it is unlikely that a large sensitivity change was introduced to the measurements after the thermal reset step in the SAR protocol. Taking into account all the ESR dating results and the limitations of the SAAD protocol, especially when dealing with old samples, we consider the ages obtained with the SAR protocol to be more reliable than the SAAD protocol ages.

The ESR kinetic parameters and thermal lifetime are largely sample-dependent. The obtained kinetic parameters for the Al center fall within the range of parameters compiled by Fang & Grün (2020) and Richter et al. (2020) from ESR dating studies. The thermal lifetime for the Al center reported in this study ($4.20*10^7$ Ma) falls within the values calculated by Richter et al. (2020) from other works in the literature at the same ambient temperature conditions. The lifetime we obtained is also larger than the one calculated using the kinetic parameters from King et al. (2020) assuming a temperature of 10 °C ($3.25*10^4$ Ma). In any case, our thermal lifetime is still above 10 times the dating limit for the method (Aitken

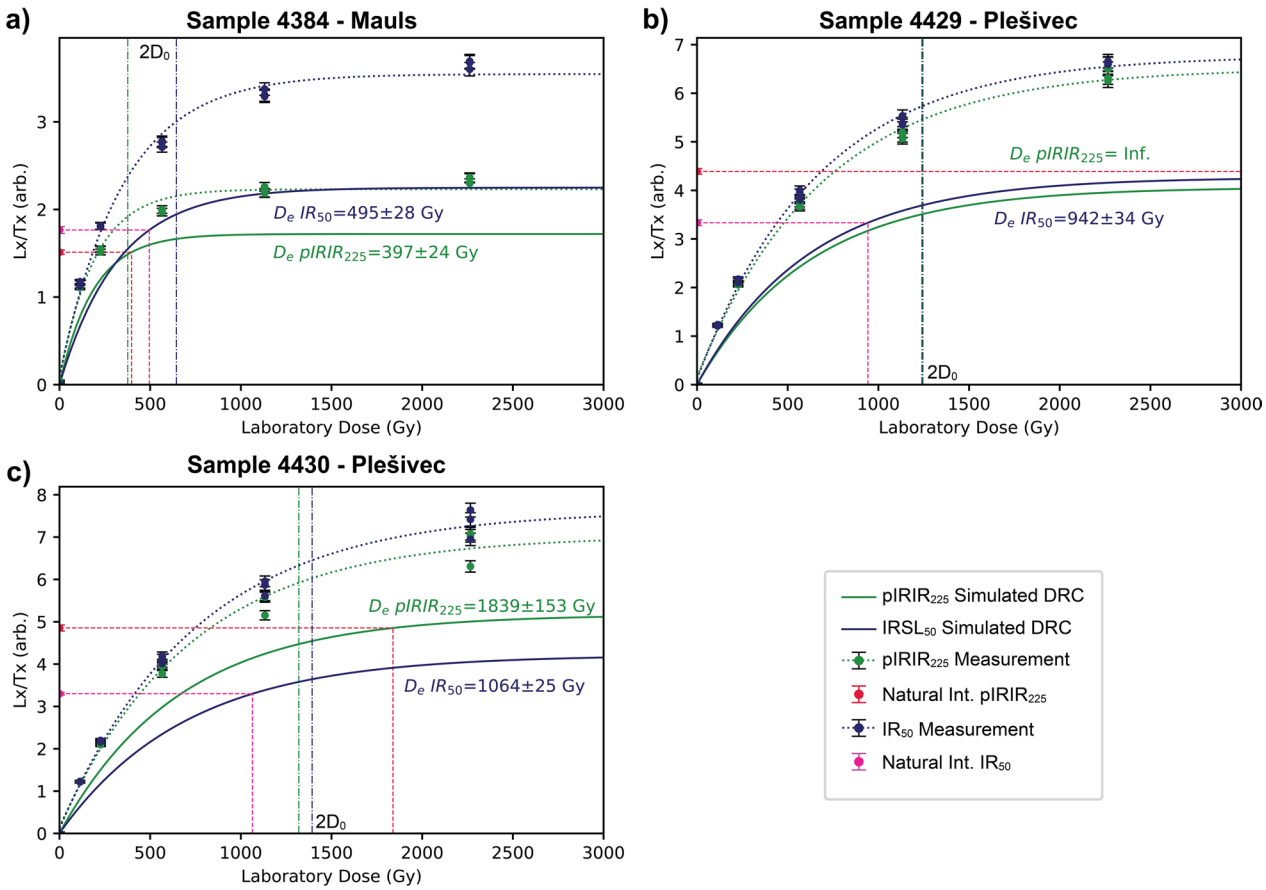

Fig. 13 OSL dose–response curves from the measured $pIRIR_{225}$ and IR_{50} signals from the samples: **a** 4384—Mauls locality, **b** 4429—Plešivec locality, **c** 4430—Plešivec locality

Table 5 Results from OSL dating measuring the $pIRIR_{225}$ and IR_{50} signals on potassium feldspar aliquots

Sample	Saturation level (%)		D_e (Gy)		$2D_0$ (Gy)		Min. age (ky)		Dose recovery ratio (residual subtraction)		Dose Recovery Ratio (No Subtraction)	
	IR_{50}	$pIRIR_{225}$	IR_{50}	$pIRIR_{225}$	IR_{50}	$pIRIR_{225}$	IR_{50}	$pIRIR_{225}$	IR_{50}	$pIRIR_{225}$	IR_{50}	$pIRIR_{225}$
4384–Mauls	78.5 ± 8.8	87.9 ± 12.9	495 ± 28	> $2D_0$	644 ± 2	376 ± 2	335 ± 21	196 ± 12	0.97 ± 0.05	0.99 ± 0.03	0.99 ± 0.05	1.00 ± 0.03
4429–Plešivec	78.3 ± 3.5	> 100	942 ± 34	Infinite	1240 ± 4	1246 ± 46	279 ± 13	281 ± 16	0.91 ± 0.01	0.93 ± 0.03	0.92 ± 0.01	0.95 ± 0.03
4430–Plešivec	78.3 ± 3.6	93.8 ± 23.2	1064 ± 25	> $2D_0$	1392 ± 4	1320 ± 4	295 ± 13	280 ± 13	0.85 ± 0.01	0.91 ± 0.01	0.85 ± 0.01	0.94 ± 0.01

1985), meaning that we can assume that no significant loss of signal due to thermal de-trapping has occurred during the last couple of million years.

Considering the results from the frictional heating experiments formulated by Yang et al. (2019), suggesting that the Al center in quartz is most likely partially reset by earthquakes of M_w 7–8, we assume that the shear heating was potentially not sufficient to fully reset the system during the last earthquakes released by the PAF. Consequently, we interpret the obtained ESR ages as the maximum ages of the last resetting event of the system, and therefore, the maximum age of the last large earthquake (Tsukamoto et al. 2020) along the specific fault segment. Still, an age overestimation due to an incomplete system reset could be accounted for by measuring multiple centers in ESR or targeting different grain size fractions (e.g., Fukuchi 1988; Schwarcz et al. 1987; Lee & Schwarcz 1994a, b; Lee 1994) while applying the SAR protocol. However, the signal from the Ti center in our samples is weak, and the centers such as E' and OHC do not strongly depend on shear heating to be effectively reset compared to the Al center (Yang et al. 2019). Therefore, only the grain size plateau approach using the Al center could still be applied. Furthermore, establishing a temperature estimate for shear heating along the fault plane is difficult. A potential way to obtain such estimates would be for instance, to measure the sensitivity changes in the OSL signal with increasing heating temperature (Rink et al. 1999), or to apply a Raman spectroscopy geothermometer for organic matter (RSCM, e.g., Kouketsu et al. 2013; Furuichi et al. 2015; Lünsdorf et al. 2017; Henry et al. 2019) on cataclasites and gouges from the fault zone.

Our results from the OSL dating show that the $pIRIR_{225}$ signals in all samples are in saturation (Table 5, Fig. 13). In the case of the IR_{50} signals, the analyzed samples are close but below saturation. However, for older samples (i.e., close to saturation) the fading correction factor for the IR_{50} signal is larger than for the $pIRIR_{225}$ signal, meaning that the corrected D_e are less reliable than those obtained for the $pIRIR_{225}$ signal. In general, other studies dealing with OSL faulting of fault gouge have identified a reset of the system associated with fault activity (e.g., Spencer et al. 2012; Tsakalos et al. 2020). However, these studies have been conducted at depth, under higher ambient temperatures and confining pressure, where the material is more likely to be effectively reset during coseismic slip. The saturated state of the measured signals could be the result of a large recurrence interval of the PAF combined with only low-magnitude events that do not fully reset the system at near-surface conditions. Another possibility would be the lack of events that effectively reset the system during the datable time range of the method. Therefore, we consider the ages calculated from the $pIRIR_{225}$ signal (Table 5) as the minimum ages of the last resetting event of the system. A potentially helpful approach to identify likely resetting of the traps would be to analyze thermoluminescence signals collectively with IRSL, as proposed by Spencer et al. (2012).

By taking advantage of the difference in saturation limits of the ESR and OSL dating methods, a combined approach using both allows us to narrow down the temporal range of the last resetting event of the system (Fig. 14) and establish whether a fault has experienced seismotectonic deformation during the Quaternary. This is useful in cases where geodetic monitoring or instruments are incapable of yielding significant data due to the slow deformation rates. In the case of the studied portion of the PAF, the obtained ages suggest that coseismic slip occurred along the fault system during the Quaternary with a maximum age for the last resetting event of the system ranging from 1075 ± 47 to 552 ± 26 ka (ESR SAR) and minimum ages in the range from 196 ± 12 to 281 ± 16 ka ($pIRIR_{225}$ using $2D_0$ estimates). The individual ages are relatively congruent (Fig. 15), and their differences could be attributed to different amounts of partial resetting of the system, differences in the timing of coseismic slip along the specific segment of the PAF, or reactivation of different fault planes as suggested by the difference in the ESR age from the Plešivec locality samples (4429 and 4430). In general, previous studies hint at fault activity

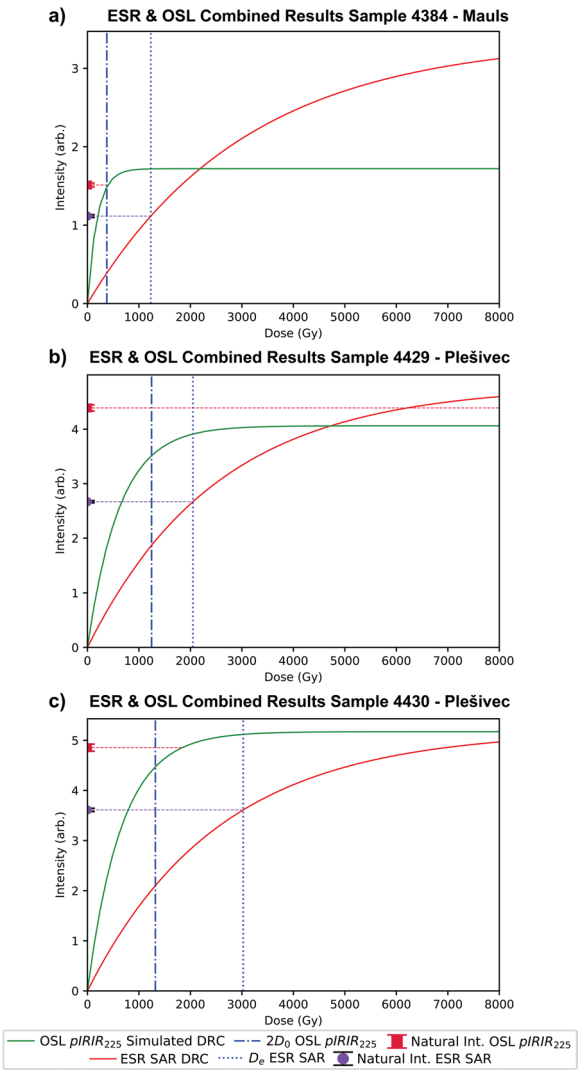

Fig. 14 Comparison between the datable range of OSL and ESR dating from the samples: **a** 4384—Mauls locality, **b** 4429—Plešivec locality, **c** 4430—Plešivec locality

along the PAF of at least Late Miocene to Pliocene age (e.g., Zwingmann and Mancktelow 2004; Heberer et al. 2017). Our findings suggest a much younger activity.

Considering most of the definitions of what makes a fault considered active, the narrowed-down period of earthquake activity we obtained for this segment of the PAF implies that by some definitions the fault cannot be determined active. Our ages cannot account for Holocene displacement (Slemmons and McKinney 1977), and although our minimum limit suggests activity younger than 0.5 Ma it is not possible to confirm how recurrent it was (U.S. National Regulatory Commission 1997). However, there are four reasons why it could be considered at least potentially active. (1) The Eastern PAF is characterized by low seismicity and low deformation rates, similar to what usually occurs in intraplate settings. According to the definition of the International Atomic Energy Agency (2010), the seismically active period we dated for the structure fits within what could be considered active for such settings. (2) Earthquake ages obtained with trapped charge dating methods are generally older than the last earthquake triggered on active faults (e.g., Fukuchi et al. 1986; Buhay et al. 1988; Tsakalos et al. 2020). They do not necessarily reflect the last coseismic slip along the structures but can still be used to assess whether a structure has been active during the Quaternary. (3) The GPS velocities displayed in Fig. 3 show there is still a transpressional component to the PAF, and the orientation of the maximum horizontal compressive stress is oriented at a high angle to PAF, but not entirely perpendicular to the structure (Aiman et al. 2023). As a consequence, low resolved shear stresses along the PAF might be the cause behind its low deformation rates, but it does not necessarily mean the structure is inactive since it could take a long time to accumulate enough strain. In addition, a very weak fault (i.e., one with low static friction, for instance, the San Andreas Fault: Carpenter et al. 2015) may slip even when principal stresses look unfavorably oriented and resolved shear stresses are low. Besides, strong historical earthquakes have occurred in the vicinity of the structure (Roman earthquake at Celje: Kazmer et al. (2023). Overall, the PAF has the potential for future offset, which is one of the criteria to identify active faults defined by several authors (Willis and Wood 1924; Slemmons and McKinney 1977; U.S. Nuclear Regulatory Commission 1997). (4) Other structures under similar tectonic settings (i.e., low deformation rates and scarce to inexistent historical and instrumental earthquake records) where earthquakes recently occurred (e.g., Provence region, France: Ritz et al. 2020; Thomas et al. 2020; Eastern US: Figueiredo et al. 2022), imply that long recurrence intervals could hinder their interpretation as active or potentially active faults. Spooner et al. (2019) have suggested that present-day seismicity with $M > 6$ events in the Alps correlates with regions of smaller crustal thickness and lower density. However, in the interior of the Alps strong historical earthquakes are documented (Stucchi et al. 2012), and additional pre-historical events have been identified in lake paleoseismology (Daxer et al. 2020, 2022a, b; Oswald et al. 2022) and cave studies (Baroň et al. 2022). These observations are in line with our findings—large earthquakes do occur in the interior of the mountain chain, but they are too rare to be captured by instrumental and historical records alone. In the regional tectonic context, an

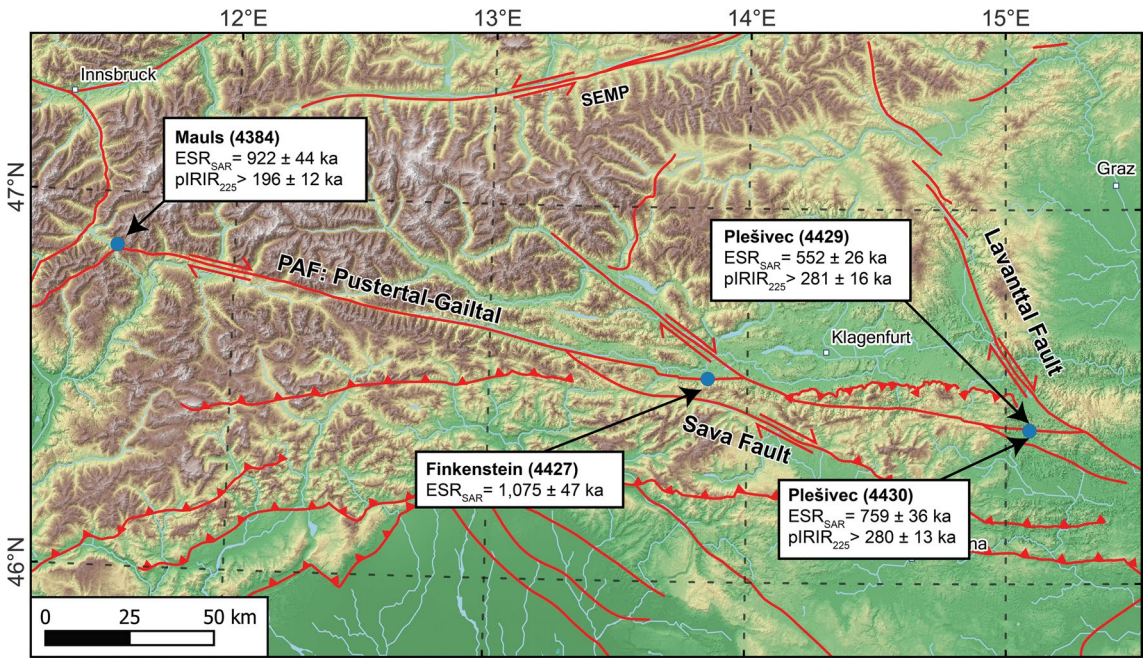

Fig. 15 Maximum (ESR SAR) and minimum (OSL pIRIR$_{225}$) ages of the last resetting event from the studied localities along the eastern PAF

active PAF will likely accommodate a small fraction of the Adria–Europe convergence, probably with a component of right-lateral slip, such as during the Neogene lateral extrusion of the Eastern Alps towards the Pannonian Basin (Ratschbacher et al. 1991a, b).

Conclusions

Trapped charge dating methods allow dating seismotectonic deformation at near-surface conditions in places where deformation rates are low or where neither instrumental nor historical earthquake records help to identify active faults. A lack of large instrumentally recorded earthquakes on the PAF system, combined with an ambiguous historical earthquake record, made the structure a suitable target to apply the methods to unravel the timing of seismotectonic deformation produced by the fault during the Quaternary. In this work, we systematically compared two available methodological approaches in ESR dating to establish a meaningful direct age of active deformation. Furthermore, we introduced the first systematic approach of combined ESR and OSL dating on quartz and feldspar from fault gouges to date active deformation. Finally, we presented the first successful attempt at absolute dating for active deformation along the PAF in the Alps.

Due to the limitations of the ESR SAAD protocol when dealing with old samples and the systematic advantages of the SAR protocol, we consider the ages obtained with the SAR protocol ages more reliable than the SAAD protocol ages. The main advantage of the SAR protocol over the SAAD protocol is a shorter uncertainty of the DRC parameters and the D_e, both associated with the lack of extrapolation for a large part of the curve. Large extrapolation steps largely affect the age calculation for aliquots with natural intensities closer to a saturated state. However, changes in sensitivity after bleaching the signal during the SAR protocol in ESR dating can be difficult to identify or quantify. Therefore, we employed a dose recovery test to verify the validity of the SAR DRC and D_e, which yielded recovery rates close to unity for most samples.

Our dating results suggest that the PAF accommodated seismotectonic deformation associated with Adria–Europe convergence during the Quaternary, with a maximum age for the last resetting event of the system (and the last large magnitude earthquake) in the range of 1075 ± 47 to 552 ± 26 ka (ESR SAR) and minimum ages in the range from 196 ± 12 to 281 ± 16 ka (pIRIR$_{225}$ using $2D_0$ estimates). Therefore, in places where activity is not so high, ESR dating on quartz could be considered the preferred method for unraveling periods of seismogenic faulting, while OSL can be additionally applied to constrain the minimum ages for the last resetting event of the system, even when the signals are in saturation. Furthermore, a combined approach of the methods allows to narrow down the timing of Quaternary seismotectonic deformation along structures where geodetic monitoring and

instruments do not yield results, such as the PAF. Considering the different definitions of what constitutes an active fault, the ages we obtained, and regional observations of the geometrical compatibility with the current stress regime, it would be possible to classify the easternmost segment of the PAF as a potentially active fault.

Abbreviations

a. u.	Arbitrary units
DRC	Dose–response curve
D_e	Equivalent dose
ESR	Electron spin resonance
GNSS	Global navigation satellite systems
IRSL	Infrared stimulated luminescence
IR_{50}	Infrared-stimulated luminescence signal released at 50 °C
OSL	Optically stimulated luminescence
PAF	Periadriatic fault
$pIRIR_{225}$	Post-infrared infrared-stimulated luminescence signal released at 225 °C
SAAD	Single aliquot additive dose
SAR	Single aliquot regenerative

Supplementary Information

The online version contains supplementary material available at https://doi.org/10.1186/s40623-024-02015-6.

Additional file 1. Complete legend of the geological map modified after Schuster et al. (2015).

Additional file 2. Additional file data of the ESR dating results. Dose response curve parameters from the applied SAR and SAAD ESR protocols.

Additional file 3. Additional file data of the Monte Carlo simulations for ESR. Comparison of the equivalent dose distributions resulting from 2000 simulations after applying the SAAD (blue distributions) and SAR (red distributions) protocols.

Additional file 4. Additional file data of the OSL dating results. Fit parameters of the laboratory dose response curves from the pIRIR225 and IR50 signals, Rho', g values, and fit parameters of the simulated natural dose response curves.

Acknowledgements

Project funding by the Deutsche Forschungsgemeinschaft (DFG), project number 442590718 awarded to ST and KU is gratefully acknowledged. The authors thank Gerlinde Ortner (GeoPark Carnic Alps) for her logistic support during fieldwork on Austrian territory, Bianca Heberer (University of Salzburg) for the discussions, the laboratory technicians at LIAG—Hannover for their help and advice in sample preparation and gamma spectrometry, Georgina King (University of Lausanne) for providing the ESR MATLAB Toolbox, the AlpArray and 4DMB communities for the discussions, Muriel Bülhoff, Mark Mücklisch, Jakob Stubenrauch and other student helpers for their involvement during the field campaigns. Finally, we would like to thank the editors of the journal and the two anonymous reviewers for their valuable comments and suggestions, which helped to improve the quality of the manuscript.

Author contributions

Erick Prince: Conception and design of the work; samples/field data acquisition; acquisition, analysis, and interpretation of data; draft of the manuscript. Sumiko Tsukamoto: Conception and design of the work; samples/field data acquisition; assistance with interpretation of data; revisions to the manuscript. Christoph Grützner: Samples/field data acquisition; assistance with interpretation of data; revisions to the manuscript. Marko Vrabec: Samples/field data acquisition; revisions to the manuscript. Kamil Ustaszewski: Conception and design of the work; samples/field data acquisition; assistance with interpretation of data; revisions to the manuscript.

Funding

Open Access funding enabled and organized by Projekt DEAL. Project funding by the Deutsche Forschungsgemeinschaft (DFG), project number 442590718 awarded to Sumiko Tsukamoto and Kamil Ustaszewski.

Availability of data and materials

The authors declare all data supporting the study are available in the document and the supplementary files. The datasets used and/or analyzed during the current study are also available from the corresponding author upon reasonable request.

Declarations

Competing interests

The authors declare there are no competing interests.

Author details

[1]Institute for Geosciences, Friedrich-Schiller University Jena, Burgweg 11, 07749 Jena, Germany. [2]Leibniz Institute for Applied Geophysics LIAG Hannover, Stilleweg 2, 30655 Hannover, Germany. [3]Department of Geosciences, Eberhard Karls University Tübingen, Schnarrenbergstr. 94-96, 72076 Tübingen, Germany. [4]University of Ljubljana, Aškerčeva cesta 12, 1000 Ljubljana, Slovenia.

Received: 31 July 2023 Accepted: 24 April 2024
Published online: 12 June 2024

References

Agency of the Republic of Slovenia for the Environment ARSO (2021). Digital terrain model 1 metre raster Slovenia. https://gis.arso.gov.si/evode/profile.aspx?id=atlas_voda_Lidar@Arso

Aiman YA, Delorey AA, Lu Y, Bokelmann G (2023) SHmax orientation in the Alpine region from observations of stress-induced anisotropy of nonlinear elasticity. Geophys J Int 235(3):2137–2148. https://doi.org/10.1093/gji/ggad353

Aitken MJ (1985) Thermoluminescence Dating. Academic Press, Cambridge

Aitken MJ (1998) An introduction to optical dating. Oxford University Press, Oxford

Albini P, Locati M, Rovida A, Stucchi M (2013) European archive of historical EArthquake data (AHEAD). Istituto Nazionale Di Geofisica e Vulcanologia (INGV). https://doi.org/10.6092/ingv.it-ahead

Anderle N (1977) 200 Arnoldstein 1:50000 Austria. Geologische Bundesanstalt Österreich, Vienna

Anderle, N. (1977b). 201 Villach—Assling 1:50.000. Geologische Bundesanstalt Österreich. Austria

Bagagli M, Molinari I, Diehl T, Kissling E, Giardini D, Clinton J, Scarabello L, Käestli P, Racine R, Massin F, Pahor J, Živčić M, Plenefisch T, Jia Y, Csicsay K, Ivančić I, Hetényi G, Abreu R, Allegretti I, Zieke T (2022) The AlpArray research seismicity-catalogue. Geophysical J Int 231(2):921–943. https://doi.org/10.1093/gji/ggac226

Baroň I, Plan L, Grasemann B, Melichar R, Mitrović-Woodell I, Rowberry M, Scholz D (2022) Three large prehistoric earthquakes in the Eastern Alps evidenced by cave rupture and speleothem damage. Geomorphology. https://doi.org/10.1016/j.geomorph.2022.108242

Beerten K, Rittner S, Lomax J, Radtke U (2008) Dose recovery tests using Ti-related ESR signals in quartz: First results. Quat Geochronol 3(1–2):143–149. https://doi.org/10.1016/j.quageo.2007.05.002

Bigi G., Castellarin A., Coli M., Dal Piaz G.V., Sartori R., Scandone P. & Vai G.B., (1990a). Structural Model of Italy scale 1:500.000, sheet 1. C.N.R., Progetto Finalizzato Geodinamica, SELCA Firenze.

Bigi G., Castellarin A., Coli M., Dal Piaz G.V. & Vai G.B., (1990b). Structural Model of Italy scale 1:500.000, sheet 2. C.N.R., Progetto Finalizzato Geodinamica, SELCA Firenze.

Brennan BJ (2003) Beta doses to spherical grains. Radiat Meas 37(4–5):299–303. https://doi.org/10.1016/s1350-4487(03)00011-8

Brennan BJ, Lyons RG, Phillips SW (1991) Attenuation of alpha particle track dose for spherical grains. Int J Rad Appl Instr Part D Nucl Tracks

Radiation Measure 18(1–2):249–253. https://doi.org/10.1016/1359-0189(91)90119-3
Buhay WM, Schwarcz HP, Grün R (1988) ESR dating of fault gouge: the effect of grain size. Quatern Sci Rev 7(3–4):515–522. https://doi.org/10.1016/0277-3791(88)90055-8
Buylaert JP, Murray AS, Thomsen KJ, Jain M (2009) Testing the potential of an elevated temperature IRSL signal from K-feldspar. Radiat Meas 44(5–6):560–565. https://doi.org/10.1016/j.radmeas.2009.02.007
Caracciolo CH, Slejko D, Camassi R, Castelli V (2021) The eastern Alps earthquake of 25 January 1348: new insights from old sources. Bull Geophys Oceanogr 63(3):335–364. https://doi.org/10.4430/bgo00364
Carpenter BM, Saffer DM, Marone C (2015) Frictional properties of the active San Andreas fault at SAFOD: Implications for fault strength and slip behavior. J Geophys Res Solid Earth 120(7):5273–5289. https://doi.org/10.1002/2015JB011963
Castellarin A, Cantelli L (2000) Neo-Alpine evolution of the Southern Eastern Alps. J Geodynamics 30(1–2):251–274. https://doi.org/10.1016/S0264-3707(99)00036-8
Cheloni D, D'Agostino N, Selvaggi G (2014) Interseismic coupling, seismic potential, and earthquake recurrence on the southern front of the Eastern Alps (NE Italy). J Geophys Res Solid Earth 119(5):4448–4468. https://doi.org/10.1002/2014jb010954
D'Agostino N, Avallone A, Cheloni D, D'Anastasio E, Mantenuto S, Selvaggi G (2008) Active tectonics of the Adriatic region from GPS and earthquake slip vectors. J Geophys Res. https://doi.org/10.1029/2008jb005860
Daxer C, Sammartini M, Molenaar A, Piechl T, Strasser M, Moernaut J (2020) Morphology and spatio-temporal distribution of lacustrine mass-transport deposits in Wörthersee, Eastern Alps, Austria. Geol Soc London Special Publ 500(1):235–254. https://doi.org/10.1144/sp500-2019-179
Daxer C, Huang JS, Weginger S, Hilbe M, Strasser M, Moernaut J (2022a) Validation of seismic hazard curves using a calibrated 14 ka lacustrine record in the Eastern Alps. Austria Sci Rep 12(1):19943. https://doi.org/10.1038/s41598-022-24487-w
Daxer C, Ortler M, Fabbri SC, Hilbe M, Hajdas I, Dubois N, Piechl T, Hammerl C, Strasser M, Moernaut J (2022) High-resolution calibration of seismically-induced lacustrine deposits with historical earthquake data in the Eastern Alps (Carinthia, Austria). Quatern Sci Rev. https://doi.org/10.1016/j.quascirev.2022.107497
Fang F, Grün R (2020) ESR thermochronometry of Al and Ti centres in quartz: a case study of the Fergusons Hill-1 borehole from the Otway Basin Australia. Radiation Measure. https://doi.org/10.1016/j.radmeas.2020.106447
Figueiredo P, Hill J, Merschat A, Scheip C, Stewart K, Owen L, Wooten R, Carter M, Szymanski E, Horton S, Wegmann K, Bohnenstiehl D, Thompson G, Witt A, Cattanach B (2022) The Mw 51, 9 August 2020, Sparta Earthquake, North Carolina: the first documented seismic surface rupture in the Eastern United States. GSA Today 32(3–4):4–11. https://doi.org/10.1130/gsatg517a.1
Fodor L, Jelen B, Márton E, Skaberne D, Čar J, Vrabec M (1998) Miocene-Pliocene tectonic evolution of the Slovenian Periadriatic fault: implications for Alpine-Carpathian extrusion models. Tectonics 17(5):690–709. https://doi.org/10.1029/98tc01605
Fukuchi T (1988) Applicability of ESR dating using multiple centres to fault movement—the case of the Itoigawa-Shizuoka tectonic line, a major fault in Japan. Quatern Sci Rev 7(3–4):509–514. https://doi.org/10.1016/0277-3791(88)90054-6
Fukuchi T (1989) Theoretical study on frictional heat by faulting using ESR international journal of radiation applications and instrumentation part a. Appl Rad Isotopes 40(10–12):1181–1193. https://doi.org/10.1016/0883-2889(89)90061-0
Fukuchi T (1992) ESR studies for absolute dating of fault movements. J Geol Soc 149(2):265–272. https://doi.org/10.1144/gsjgs.149.2.0265
Fukuchi T (2001) Assessment of fault activity by ESR dating of fault gouge; an example of the 500 m core samples drilled into the Nojima earthquake fault in Japan. Quatern Sci Rev 20(5–9):1005–1008. https://doi.org/10.1016/s0277-3791(00)00064-0
Fukuchi T, Imai N, Shimokawa K (1986) ESR dating of fault movement using various defect centres in quartz; the case in the western South Fossa Magna. Japan Earth Planet Sci Lett 78(1):121–128. https://doi.org/10.1016/0012-821x(86)90178-0
Furuichi H, Ujiie K, Kouketsu Y, Saito T, Tsutsumi A, Wallis S (2015) Vitrinite reflectance and Raman spectra of carbonaceous material as indicators of frictional heating on faults: constraints from friction experiments. Earth Planet Sci Lett 424:191–200. https://doi.org/10.1016/j.epsl.2015.05.037
Geološki zavod Slovenije. (2003). Basic geological map of Yugoslavia 1:100000. https://eprostor.gov.si/imps/srv/api/records/2d6837af-90a4-46c4-bed7-87a2ebf41d0e
Grünthal G, Wahlström R (2012) The European-Mediterranean Earthquake Catalogue (EMEC) for the last millennium. J Seismol 16(3):535–570. https://doi.org/10.1007/s10950-012-9302-y
Grützner C, Fischer P, Reicherter K (2016) Holocene surface ruptures of the rurrand fault, Germany—insights from palaeoseismology, remote sensing and shallow geophysics. Geophys J Int 204(3):1662–1677. https://doi.org/10.1093/gji/ggv558
Grützner C, Carson E, Walker RT, Rhodes EJ, Mukambayev A, Mackenzie D, Elliott JR, Campbell G, Abdrakhmatov K (2017) Assessing the activity of faults in continental interiors: Palaeoseismic insights from SE Kazakhstan. Earth Planet Sci Lett 459:93–104. https://doi.org/10.1016/j.epsl.2016.11.025
Grützner C, Aschenbrenner S, Jamšek R, P, Reicherter, K, Saifelislam, N, Vičič, B, Vrabec, M, Welte, J, & Ustaszewski, K. (2021) Holocene surface-rupturing earthquakes on the Dinaric Fault System, western Slovenia. Solid Earth 12(10):2211–2234. https://doi.org/10.5194/se-12-2211-2021
Guérin G, Mercier N, Nathan R, Adamiec G, Lefrais Y (2012) On the use of the infinite matrix assumption and associated concepts: a critical review. Radiat Meas 47(9):778–785. https://doi.org/10.1016/j.radmeas.2012.04.004
Guidoboni E, Ferrari G, Tarabusi G, Sgattoni G, Comastri A, Mariotti D, Ciuccarelli C, Bianchi MG, Valensise G (2019) CFTI5Med, the new release of the catalogue of strong earthquakes in Italy and in the Mediterranean area. Sci Data 6(1):80. https://doi.org/10.1038/s41597-019-0091-9
Guralnik B, Jain M, Herman F, Ankjærgaard C, Murray AS, Valla PG, Preusser F, King GE, Chen R, Lowick SE, Kook M, Rhodes EJ (2015) OSL-thermochronometry of feldspar from the KTB borehole, Germany. Earth Planet Sci Lett 423:232–243. https://doi.org/10.1016/j.epsl.2015.04.032
Hammerl, C., Albini, P., & Moroni, A. (1994). The earthquake of January 25th, 1348: discussion of sources. Historical investigation of European earthquakes.
Handy MR, Babist J, Wagner R, Rosenberg CL, Konrad M (2005) Decoupling and its relation to strain partitioning in continental lithosphere: insight from the Periadriatic fault system (European Alps). Geol Soc London Special Publ 243(1):249–276. https://doi.org/10.1144/gsl.Sp.2005.243.01.17
Heberer B, Reverman RL, Fellin MG, Neubauer F, Dunkl I, Zattin M, Seward D, Genser J, Brack P (2017) Postcollisional cooling history of the Eastern and Southern Alps and its linkage to Adria indentation. Int J Earth Sci 106(5):1557–1580. https://doi.org/10.1007/s00531-016-1367-3
Henry DG, Jarvis I, Gillmore G, Stephenson M (2019) Raman spectroscopy as a tool to determine the thermal maturity of organic matter: application to sedimentary, metamorphic and structural geology. Earth-Sci Rev. https://doi.org/10.1016/j.earscirev.2019.102936
Hetényi G, Plomerová J, Bianchi I, Kampfová Exnerová H, Bokelmann G, Handy MR, Babuška V (2018) From mountain summits to roots: crustal structure of the Eastern Alps and Bohemian Massif along longitude 13.3°E. Tectonophysics 744:239–255. https://doi.org/10.1016/j.tecto.2018.07.001
Hintersberger E, Decker K, Lomax J, Lüthgens C (2018) Implications from palaeoseismological investigations at the Markgrafneusiedl Fault (Vienna Basin, Austria) for seismic hazard assessment. Nat Hazard 18(2):531–553. https://doi.org/10.5194/nhess-18-531-2018
Hiraga S, Morimoto A, Shimamoto T (2002) Stress effect on thermoluminescence intensities of quartz grain—for the establishment of a fault dating method-. Bull Nara Univ Educ 51(2):17–24
Huntley DJ (2006) An explanation of the power-law decay of luminescence. J Phys-Condensed Matter 18(4):1359–1365. https://doi.org/10.1088/0953-8984/18/4/020
Huntley DJ, Baril MR (1997) The K content of the K-feldspars being measured in optical dating or in thermoluminescence dating. Ancient TL 15(1):11–13

I. A. E. Agency. (2010). Seismic hazards in site evaluation for nuclear installations, Safety Standards Series No. SSG-9, p. 60, http://www-ns.iaea.org/standards/.
Ikeya M, Miki T, Tanaka K (1982) Dating of a fault by electron spin resonance on intrafault materials. Science 215(4538):1392–1393. https://doi.org/10.1126/science.215.4538.1392
Jozi Najafabadi A, Haberland C, Ryberg T, Verwater VF, Le Breton E, Handy MR, Weber M (2021) Relocation of earthquakes in the southern and eastern Alps (Austria, Italy) recorded by the dense, temporary SWATH-D network using a Markov chain Monte Carlo inversion. Solid Earth 12(5):1087–1109. https://doi.org/10.5194/se-12-1087-2021
NASA JPL (2013). NASA Shuttle Radar Topography Mission Global 1 arc second NASA EOSDIS Land processes distributed active archive center. Accessed 2023-07-30 from https://doi.org/10.5067/MEaSUREs/SRTM/SRTMGL1.003
KAGIS. (2020). Digital elevation model Carinthia. https://gis.ktn.gv.at/webgisviewer/atlas-mobile/map/Basiskarten/H%C3%B6heninformation
Kars RH, Wallinga J, Cohen KM (2008) A new approach towards anomalous fading correction for feldspar IRSL dating-tests on samples in field saturation. Radiation Measure 43:786–790. https://doi.org/10.1016/j.radmeas.2008.01.021
Kázmér M, Jamšek Rupnik P, Gaidzik K (2023) Seismic activity in the Celje Basin (Slovenia) in roman times—archaeoseismological evidence from Celeia. Quaternary 6(1):10. https://doi.org/10.3390/quat6010010
Kim JH, Ree J-H, Choi J-H, Chauhan N, Hirose T, Kitamura M (2019) Experimental investigations on dating the last earthquake event using OSL signals of quartz from fault gouges. Tectonophysics. https://doi.org/10.1016/j.tecto.2019.228191
King GE, Tsukamoto S, Herman F, Biswas RH, Sueoka S, Tagami T (2020) Electron spin resonance (ESR) thermochronometry of the Hida range of the Japanese Alps: validation and future potential. Geochronology 2(1):1–15. https://doi.org/10.5194/gchron-2-1-2020
King TR, Quigley M, Clark D, Zondervan A, May JH, Alimanovic A (2021) Paleoseismology of the 2016 MW 61 Petermann earthquake source: Implications for intraplate earthquake behaviour and the geomorphic longevity of bedrock fault scarps in a low strain-rate cratonic region. Earth Surf Process Landforms 46(7):1238–1256. https://doi.org/10.1002/esp.5090
Kondo H, Owen LA, Figueiredo PM (2022) Paleoseismological studies. Treatise Geomorphol. https://doi.org/10.1016/B978-0-12-818234-5.00156-5
Kouketsu Y, Mizukami T, Mori H, Endo S, Aoya M, Hara H, Nakamura D, Wallis S (2013) A new approach to develop theRaman carbonaceous material geothermometer for low-grade metamorphism using peak width. Island Arc 23(1):33–50. https://doi.org/10.1111/iar.12057
Kralik M, Klima K, Riedmüller G (1987) Dating fault gouges. Nature 327(6120):315–317. https://doi.org/10.1038/327315a0
Kreutzer S, Schmidt C, Fuchs MC, Dietze M, Fischer M, Fuchs M (2012) Introducing an R package for luminescence dating analysis. Ancient TL 30(1):1–8
Lambert R (2018) Investigating thermal decay in K-feldspar for the application of IRSL thermochronometry on the Mont Blanc massif. University of Lausanne, Lausanne
Laubscher HP (1971) The large-scale kinematics of the western Alps and the northern Apennines and its palinspastic implications. Am J Sci 271(3):193–226. https://doi.org/10.2475/ajs.271.3.193
Lee HK (1994) ESR dating of fault rocks. McMaster University, Hamilton
Lee HK, Schwarcz EP (1993) An experimental study of shear-induced zeroing of ESR signals in quartz. Appl Radiat Isot 44(1–2):191–195. https://doi.org/10.1016/0969-8043(93)90218-y
Lee HK, Schwarcz HP (1994a) Criteria for complete zeroing of ESR signals during faulting of the San Gabriel fault zone, southern California. Tectonophysics 235(4):317–337. https://doi.org/10.1016/0040-1951(94)90192-9
Lee HK, Schwarcz HP (1994b) ESR plateau dating of fault gouge. Quatern Sci Rev 13(5–7):629–634. https://doi.org/10.1016/0277-3791(94)90090-6
Lee, H.-K., & Schwarcz, H. P. (1996). Electron spin resonance plateau dating of periodicity of activity on the San Gabriel fault zone, southern California GSA. Bulletin 108(6) 735–746
Lee, H.-K. (1995). ESR Plateau dating of fault rocks McMaster University. Ontario
Liritzis I, Stamoulis K, Papachristodoulou C, Ioannides K (2012) A re-evaluation of radiation dose-rate conversion factors. Mediterranean Archaeol Archaeom 13(3):1–15. https://doi.org/10.1007/978-3-319-00170-8_3
Lünsdorf NK, Dunkl I, Schmidt BC, Rantitsch G, von Eynatten H (2017) Towards a higher comparability of geothermometric data obtained by raman spectroscopy of carbonaceous material part 2: a revised geothermometer. Geostand Geoanal Res 41(4):593–612. https://doi.org/10.1111/ggr.12178
Machette MN (2000) Active, capable, and potentially active faults—a paleoseismic perspective. J Geodyn 29(3–5):387–392. https://doi.org/10.1016/s0264-3707(99)00060-5
Mahan SA, Rittenour TM, Nelson MS, Ataee N, Brown N, DeWitt R, Durcan J, Evans M, Feathers J, Frouin M, Guérin G, Heydari M, Huot S, Jain M, Keen-Zebert A, Li B, López GI, Neudorf C, Porat N, Thomsen K (2022) Guide for interpreting and reporting luminescence dating results. GSA Bull. https://doi.org/10.1130/b36404.1
Matsumoto H, Yamanaka C, Ikeya M (2008) ESR analysis of the Nojima fault gouge, Japan, from the DPRI 500 m borehole. Island Arc 10(3–4):479–485. https://doi.org/10.1111/j.1440-1738.2001.00346.x
McCalpin JP (2009) Paleoseismology. Elsevier, Amsterdam
Merlini S, Doglioni C (2002) Analisi strutturale lungo un prolo geologico fra la linea Fella-Sava e l'avampaese adriatico (Friuli - Venezia Giulia - Italia). Mem Soc Geol It 57(293):300
Métois M, D'Agostino N, Avallone A, Chamot-Rooke N, Rabaute A, Duni L, Kuka N, Koci R, Georgiev I (2015) Insights on continental collisional processes from GPS data: dynamics of the peri-Adriatic belts. J Geophys Res Solid Earth 120(12):8701–8719. https://doi.org/10.1002/2015jb012023
Miki T, Ikeya M (1982) Physical basis of fault dating with ESR. Naturwissenschaften 69:90–91
Moulin A, Benedetti L (2018) Fragmentation of the adriatic promontory: new chronological constraints from neogene shortening rates across the Southern Alps (NE Italy). Tectonics 37(9):3328–3348. https://doi.org/10.1029/2018tc004958
Murray AS, Wintle AG (2000) Luminescence dating of quartz using an improved single-aliquot regenerative-dose protocol. Radiat Meas 32(1):57–73. https://doi.org/10.1016/s1350-4487(99)00253-x
Nemes F, Neubauer F, Cloetingh S, Genser J (1997) The Klagenfurt Basin in the Eastern Alps: an intra-orogenic decoupled flexural basin? Tectonophysics 282(1–4):189–203. https://doi.org/10.1016/s0040-1951(97)00219-9
Nuriel P, Rosenbaum G, Zhao J-X, Feng Y, Golding SD, Villemant B, Weinberger R (2012) U-Th dating of striated fault planes. Geology 40(7):647–650. https://doi.org/10.1130/g32970.1
Nussbaum C (2000) Neogene tectonics and thermal maturity of sediments of the easternmost Southern Alps (Friuli Area, Italy). Université de Neuchâtel, Neuchâtel
Oohashi K, Minomo Y, Akasegawa K, Hasebe N, Miura K (2020) Optically stimulated luminescence signal resetting of quartz gouge during subseismic to seismic frictional sliding a case study using granite-derived Quartz. J Geophys Res Solid Earth. https://doi.org/10.1029/2020jb019900
Oppermann F, Tsukamoto S (2015) A portable system of X-ray irradiation and heating for electron spin resonance. Ancient TL 33(1):11–15
Oswald P, Strasser M, Skapski J, Moernaut J (2022) Magnitude and source area estimations of severe prehistoric earthquakes in the western Austrian Alps. Nat Hazard 22(6):2057–2079. https://doi.org/10.5194/nhess-22-2057-2022
Pleuger J, Mancktelow N, Zwingmann H, Manser M (2012) K-Ar dating of synkinematic clay gouges from Neoalpine faults of the Central, Western and Eastern Alps. Tectonophysics 550–553:1–16. https://doi.org/10.1016/j.tecto.2012.05.001
Polinski RK, Eisbacher GH (1992) Deformation partitioning during polyphase oblique convergence in the Karawanken Mountains, southeastern Alps. J Struct Geol 14(10):1203–1213. https://doi.org/10.1016/0191-8141(92)90070-d
Pomella H, Stipp M, Fügenschuh B (2012) Thermochronological record of thrusting and strike-slip faulting along the Giudicarie fault system (Alps, Northern Italy). Tectonophysics 579:118–130. https://doi.org/10.1016/j.tecto.2012.04.015
Prescott JR, Hutton JT (1994) Cosmic ray contributions to dose rates for luminescence and ESR dating: large depths and long-term time variations. Radiat Meas 23(2–3):497–500. https://doi.org/10.1016/1350-4487(94)90086-8
Preusser F, Degering D, Fuchs M, Hilgers A, Kadereit A, Klasen N, Krbetschek M, Richter D, Spencer JQG (2008) Luminescence dating: basics, methods

and applications. E&G Quatern Sci J 57(1/2):95–149. https://doi.org/10.3285/eg.57.1-2.5
Rajendran CP, Rajendran K, Thakkar M, Goyal B (2008) Assessing the previous activity at the source zone of the 2001 Bhuj earthquake based on the near-source and distant paleoseismological indicators. J Geophys Res. https://doi.org/10.1029/2006jb004845
Ratschbacher L, Merle O, Davy P, Cobbold P (1991a) Lateral extrusion in the eastern Alps, part 1: boundary conditions and experiments scaled for gravity. Tectonics 10(2):245–256. https://doi.org/10.1029/90tc02622
Ratschbacher L, Frisch W, Linzer H-G, Merle O (1991b) Lateral extrusion in the eastern Alps, part 2: structural analysis. Tectonics 10(2):257–271. https://doi.org/10.1029/90tc02623
Readhead ML (2002) Absorbed dose fraction for 87Rb β particles. Ancient TL 20(1):25–28
Reiter F, Freudenthaler C, Hausmann H, Ortner H, Lenhardt W, Brandner R (2018) Active seismotectonic deformation in front of the dolomites indenter. Eastern Alps Tectonics 37(12):4625–4654. https://doi.org/10.1029/2017tc004867
Richter M, Tsukamoto S (2022) Investigation of quartz electron spin resonance residual signals in the last glacial and early Holocene fluvial deposits from the Lower Rhine. Geochronology 4(1):55–63. https://doi.org/10.5194/gchron-4-55-2022
Richter M, Tsukamoto S, Long H (2020) ESR dating of Chinese loess using the quartz Ti centre: a comparison with independent age control. Quatern Int 556:159–164. https://doi.org/10.1016/j.quaint.2019.04.003
Richter M, Tsukamoto S, Chapot MS, Duller GAT, Barham LS (2022) Electron spin resonance dating of quartz from archaeological sites at Victoria Falls Zambia. Quatern Geochronol. https://doi.org/10.1016/j.quageo.2022.101345
Ring U, Uysal IT, Glodny J, Cox SC, Little T, Thomson SN, Stübner K, Bozkaya Ö (2017) Fault-gouge dating in the Southern Alps, New Zealand. Tectonophysics 717:321–338. https://doi.org/10.1016/j.tecto.2017.08.007
Rink WJ (1997) Electron spin resonance (ESR) dating and ESR applications in quaternary science and archaeometry. Radiat Meas 27(5–6):975–1025. https://doi.org/10.1016/s1350-4487(97)00219-9
Rink WJ, Toyoda S, Rees-Jones J, Schwarcz HP (1999) Thermal activation of OSL as a geothermometer for quartz grain heating during fault movements. Radiat Meas 30(1):97–105. https://doi.org/10.1016/s1350-4487(98)00095-x
Ritz J-F, Baize S, Ferry M, Larroque C, Audin L, Delouis B, Mathot E (2020) Surface rupture and shallow fault reactivation during the 2019 Mw 49 Le Teil earthquake. Communications Earth & Environment, France. https://doi.org/10.1038/s43247-020-0012-z
Rockenschaub M, Nowotny A (2011) 175 Sterzing 1:50000. Geologische Bundesanstalt Österreich, Vienna
Rosenberg CL (2004) Shear zones and magma ascent: a model based on a review of the Tertiary magmatism in the Alps. Tectonics. https://doi.org/10.1029/2003tc001526
Sánchez L, Völksen C, Sokolov A, Arenz H, Seitz F (2018a) Present-day surface deformation of the Alpine region inferred from geodetic techniques. Earth System Sci Data 10(3):1503–1526. https://doi.org/10.5194/essd-10-1503-2018
Sánchez, L., Völksen, C., Sokolov, A., Arenz, H., & Seitz, F. (2018b). Present-day surface deformation of the Alpine Region inferred from geodetic techniques (data). PANGAEA. https://doi.pangaea.de/10.1594/PANGAEA.886889
Schellmann G, Beerten K, Radtke U (2008) Electron spin resonance (ESR) dating of quaternary materials. E&G Quatern Sci J 57(1/2):150–178. https://doi.org/10.3285/eg.57.1-2.6
Schmid SM, Kissling E (2000) The arc of the western Alps in the light of geophysical data on deep crustal structure. Tectonics 19(1):62–85. https://doi.org/10.1029/1999tc900057
Schmid SM, Aebli HR, Heller F, Zingg A (1989) The role of the Periadriatic line in the tectonic evolution of the Alps. Geol Soc London 45(1):153–171. https://doi.org/10.1144/gsl.Sp.1989.045.01.08
Schmid SM, Fügenschuh B, Kissling E, Schuster R (2004) Tectonic map and overall architecture of the Alpine orogen. Eclogae Geol Helv 97(1):93–117. https://doi.org/10.1007/s00015-004-1113-x
Schmid SM, Scharf A, Handy MR, Rosenberg CL (2013) The Tauern Window (Eastern Alps, Austria): a new tectonic map, with cross-sections and a tectonometamorphic synthesis. Swiss J Geosci 106(1):1–32. https://doi.org/10.1007/s00015-013-0123-y
Schönborn G (1999) Balancing cross sections with kinematic constraints: The Dolomites (northern Italy). Tectonics 18(3):527–545. https://doi.org/10.1029/1998tc900018
Schuster R, Egger H, Krenmayr HG, Linner M, Mandl GW, Matura A, Nowotny A, Pascher G, Pestal G, Pistotnik J, Rockenschaub M, Schnabel W (2015) Geologische Übersichtskarte der Republik Österreich 1:1 500 000 Geological Survey of Austria. Vienna
Schwarcz, H. P., Buhay, W. M., & Grün, R. (1987). Electron spin resonance (ESR) dating of fault gouge. In: Directions in Paleoseismology, U.S.G.S. Open File Report OF 87–673 (eds Crone, A. J. and Olmdahl, E.).
Serpelloni E, Vannucci G, Anderlini L, Bennett RA (2016) Kinematics, seismotectonics and seismic potential of the eastern sector of the European Alps from GPS and seismic deformation data. Tectonophysics 688:157–181. https://doi.org/10.1016/j.tecto.2016.09.026
Serpelloni E, Cavaliere A, Martelli L, Pintori F, Anderlini L, Borghi A, Randazzo D, Bruni S, Devoti R, Perfetti P, Cacciaguerra S (2022) Surface velocities and strain-rates in the Euro-Mediterranean region from massive GPS data processing. Front Earth Sci. https://doi.org/10.3389/feart.2022.907897
Sibson RH (1977) Fault rocks and fault mechanisms. J Geol Soc 133(3):191–213. https://doi.org/10.1144/gsjgs.133.3.0191
Sibson RH (1986) Earthquakes and rock deformation in crustal fault zones. Annu Rev Earth Planet Sci 14(1):149–175. https://doi.org/10.1146/annurev.ea.14.050186.001053
Sieberer A-K, Willingshofer E, Klotz T, Ortner H, Pomella H (2023) Inversion of extensional basins parallel and oblique to their boundaries: inferences from analogue models and field observations from the Dolomites Indenter. European Eastern Southern Alps Solid Earth 14(7):647–681. https://doi.org/10.5194/se-14-647-2023
Slemmons, D. B., & McKinney, R. (1977). Definition of 'active fault'. Final report. https://www.osti.gov/biblio/7297939
Spencer JQG, Hadizadeh J, Gratier J-P, Doan M-L (2012) Dating deep? Luminescence studies of fault gouge from the San Andreas Fault zone 2.6 km beneath Earth's surface. Quat Geochronol 10:280–284. https://doi.org/10.1016/j.quageo.2012.04.023
Spooner C, Scheck-Wenderoth M, Götze H-J, Ebbing J, Hetényi G (2019) Density distribution across the Alpine lithosphere constrained by 3-D gravity modelling and relation to seismicity and deformation. Solid Earth 10(6):2073–2088. https://doi.org/10.5194/se-10-2073-2019
Stucchi M, Rovida A, Gomez Capera AA, Alexandre P, Camelbeeck T, Demircioglu MB, Gasperini P, Kouskouna V, Musson RMW, Radulian M, Sesetyan K, Vilanova S, Baumont D, Bungum H, Fäh D, Lenhardt W, Makropoulos K, Martinez Solares JM, Scotti O, Giardini D (2012) The SHARE European Earthquake Catalogue (SHEEC) 1000–1899. J Seismol 17(2):523–544. https://doi.org/10.1007/s10950-012-9335-2
Takeuchi A, Ongirad H, Akimitsu T (2003) Recurrence interval of big earthquakes along the Atotsugawa fault system, central Japan: results of seismo-geological survey. Geophys Res Lett. https://doi.org/10.1029/2002gl014957
Thomas F, Rizza M, Bellier O, Billant J, Dussouillez P, Fleury J, Delanghe D, Ollivier V, Godard V, Talon B (2020) Assessing post-pliocene deformation in a context of slow tectonic deformation: insights from paleoseismology, remote sensing and shallow geophysics in Provence. France Natural Hazards 105(2):1453–1490. https://doi.org/10.1007/s11069-020-04362-5
Thomsen KJ, Jain M, Murray AS, Denby PM, Roy N, Bøtter-Jensen L (2008) Minimizing feldspar OSL contamination in quartz UV-OSL using pulsed blue stimulation. Radiat Meas 43(2–6):752–757. https://doi.org/10.1016/j.radmeas.2008.01.020
Torgersen E, Viola G, Zwingmann H, Harris C (2014) Structural and temporal evolution of a reactivated brittle-ductile fault—part ii: timing of fault initiation and reactivation by K-Ar dating of synkinematic illite/muscovite. Earth Planet Sci Lett 407:221–233. https://doi.org/10.1016/j.epsl.2014.09.031
Toyoda S, Ikeya M (1991) Thermal stabilities of paramagnetic defect and impurity centers in quartz: basis for ESR dating of thermal history. Geochem J 25(6):437–445. https://doi.org/10.2343/geochemj.25.437
Toyoda S, Miura H, Tissoux H (2009) Signal regeneration in ESR dating of tephra with quartz. Radiat Meas 44(5–6):483–487. https://doi.org/10.1016/j.radmeas.2009.03.002

Tsakalos E, Lin A, Kazantzaki M, Bassiakos Y, Nishiwaki T, Filippaki E (2020) Absolute dating of past seismic events using the OSL technique on fault gouge material a case study of the Nojima Fault Zone SW Japan. J Geophys Res Solid Earth. https://doi.org/10.1029/2019jb019257
Tsukamoto S, Toyoda S, Tani A, Oppermann F (2015) Single aliquot regenerative dose method for ESR dating using X-ray irradiation and preheat. Radiat Meas 81:9–15. https://doi.org/10.1016/j.radmeas.2015.01.018
Tsukamoto S, Porat N, Ankjærgaard C (2017) Dose recovery and residual dose of quartz ESR signals using modern sediments: Implications for single aliquot ESR dating. Radiat Meas 106:472–476. https://doi.org/10.1016/j.radmeas.2017.02.010
Tsukamoto S, Long H, Richter M, Li Y, King GE, He Z, Yang L, Zhang J, Lambert R (2018) Quartz natural and laboratory ESR dose response curves: a first attempt from Chinese loess. Radiat Meas 120:137–142. https://doi.org/10.1016/j.radmeas.2018.09.008
Tsukamoto S, Tagami T, Zwingmann H (2020) Direct dating of fault movement. In: Tanner D, Brandes C (eds) Understanding faults detecting, dating, and modeling. Elsevier, Amsterdam
Tsukamoto S, Oppermann F, Autzen M, Richter M, Bailey M, Ankjærgaard C, Jain M (2021) Response of the Ti and Al electron spin resonance signals in quartz to X-ray irradiation. Radiation Measurements. https://doi.org/10.1016/j.radmeas.2021.106676
Tuttle MP, Schweig ES, Sims JD, Lafferty RH, Wolf LW, Haynes ML (2002) The earthquake potential of the New Madrid seismic zone. Bull Seismol Soc Am 92(6):2080–2089. https://doi.org/10.1785/0120010227
U. S. N. R. Commission. (1997). Regulatory Guide 1.165. Identification and characterization of seismic sources and determination of safe shutdown earthquake ground motion, U.S. Nuclear Regulatory Commission, Office of Nuclear Regulatory Research, Mar 1997.
Ustaszewski K, Schmid SM, Fügenschuh B, Tischler M, Kissling E, Spakman W (2008) A map-view restoration of the alpine-carpathian-dinaridic system for the early miocene. Swiss J Geosci 101(S1):273–294. https://doi.org/10.1007/s00015-008-1288-7
Verwater VF, Le Breton E, Handy MR, Picotti V, Jozi Najafabadi A, Haberland C (2021) Neogene kinematics of the Giudicarie Belt and eastern Southern Alpine orogenic front (northern Italy). Solid Earth 12(6):1309–1334. https://doi.org/10.5194/se-12-1309-2021
Viola G, Mancktelow NS, Seward D (2001) Late oligocene-neogene evolution of Europe-Adria collision: new structural and geochronological evidence from the giudicarie fault system (Italian Eastern Alps). Tectonics 20(6):999–1020. https://doi.org/10.1029/2001tc900021
von Blanckenburg F, Davies JH (1995) Slab breakoff: a model for syncollisional magmatism and tectonics in the Alps. Tectonics 14(1):120–131. https://doi.org/10.1029/94tc02051
Vrabec M, Fodor L (2006) Late cenozoic tectonics of slovenia: structural styles at the northeastern corner of the adriatic microplate. In: Pinter N, Gyula G, Weber J, Stein S, Medak D (eds) The Adria microplate: GPS geodesy. Tectonics and Hazards, Dordrecht
Vrolijk P, Pevear D, Covey M, LaRiviere A (2018) Fault gouge dating: history and evolution. Clay Miner 53(3):305–324. https://doi.org/10.1180/clm.2018.22
Willis B, Wood HO (1924) A fault map of California. Science 59(1527):310–311. https://doi.org/10.1126/science.59.1527.310
Wintle AG, Huntley DJ (1982) Thermoluminescence dating of sediments. Quatern Sci Rev 1(1):31–53. https://doi.org/10.1016/0277-3791(82)90018-x
Yang HL, Chen J, Yao L, Liu CR, Shimamoto T, Thompson Jobe JA (2019) Resetting of OSL/TL/ESR signals by frictional heating in experimentally sheared quartz gouge at seismic slip rates. Quat Geochronol 49:52–56. https://doi.org/10.1016/j.quageo.2018.05.005
Zwingmann H, Mancktelow N (2004) Timing of alpine fault gouges. Earth Planet Sci Lett 223(3–4):415–425. https://doi.org/10.1016/j.epsl.2004.04.041

Publisher's Note

Springer Nature remains neutral with regard to jurisdictional claims in published maps and institutional affiliations.